batteries

MDPI

Review

MXene-Based Materials for Multivalent Metal-Ion Batteries

Chunlei Wang [1], Zibing Pan [1], Huaqi Chen [1], Xiangjun Pu [2,*] and Zhongxue Chen [1,*]

[1] School of Power and Mechanical Engineering, Wuhan University, Wuhan 430072, China
[2] Department of Industrial and Systems Engineering, the Hong Kong Polytechnic University, Hung Hom, Hong Kong 999077, China
* Correspondence: xiangjun.pu@polyu.edu.hk (X.P.); zxchen_pmc@whu.edu.cn (Z.C.)

Abstract: Multivalent metal ion (Mg^{2+}, Zn^{2+}, Ca^{2+}, and Al^{3+}) batteries (MMIBs) emerged as promising technologies for large-scale energy storage systems in recent years due to the abundant metal reserves in the Earth's crust and potentially low cost. However, the lack of high-performance electrode materials is still the main obstacle to the development of MMIBs. As a newly large family of two-dimensional transition metal carbides, nitrides, and carbonitrides, MXenes have attracted growing focus in the energy storage field because of their large specific surface area, excellent conductivity, tunable interlayer spaces, and compositional diversity. In particular, the multifunctional chemistry and superior hydrophilicity enable MXenes to serve not only as electrode materials but also as important functional components for heterojunction composite electrodes. Herein, the advances of MXene-based materials since its discovery for MMIBs are summarized, with an emphasis on the rational design and controllable synthesis of MXenes. More importantly, the fundamental understanding of the relationship between the morphology, structure, and function of MXenes is highlighted. Finally, the existing challenges and future research directions on MXene-based materials toward MMIBs application are critically discussed and prospected.

Keywords: MXenes; composite materials; multivalent metal-ion batteries

check for updates

Citation: Wang, C.; Pan, Z.; Chen, H.; Pu, X.; Chen, Z. MXene-Based Materials for Multivalent Metal-Ion Batteries. *Batteries* **2023**, *9*, 174. https://doi.org/10.3390/batteries9030174

Academic Editor: Birger Horstmann

Received: 29 January 2023
Revised: 11 March 2023
Accepted: 14 March 2023
Published: 17 March 2023

1. Introduction

Driven by the global carbon peaking and carbon neutrality goals, more and more attention has been focused on abundant and clean renewable energy sources, such as wind energy and solar energy [1,2]. However, these energy resources suffer from intermittent volatility; thus, they cannot meet the stability and reliability requirements of the rigid grid [3]. The lithium-ion battery is widely accepted as the suitable energy storage device to bridge renewable energy power generation to the power grid due to its high-energy density, long lifetime, and fast response capability, but it is plagued by increasing costs and safety issues [4]. In this regard, exploring alternative electrochemical energy storage technologies is particularly urgent. Magnesium, zinc, calcium, and aluminum metals are all Earth-abundant elements, and their redox reactions are always accompanied by a two or three electron transfer; hence, batteries based on these metal anodes in theory can offer much higher capacity than lithium-ion batteries [5,6]. Inspired by the above advantages, the research of multivalent metal ion (Mg^{2+}, Zn^{2+}, Ca^{2+}, and Al^{3+}) batteries (MMIBs) has flourished. However, the development of MMIBs is hindered by several critical issues. Firstly, the large radius of hydrated ions slows the solid-phase ion diffusion kinetics of carriers in the electrode material, resulting in severe attenuation of battery performance [7]. Secondly, the high electrostatic repulsion between the inserted cations and the host structure often leads to drastic structural deterioration and capacity decay [8]. Therefore, on the basis of good conductivity, small loss and easy modeling of general electrode materials, MMIB electrode materials also need to have a wide ion diffusion channel and sufficient structural stability to adapt to the enhanced electrostatic effect.

Two-dimensional (2D) materials have exotic electronic, chemical, mechanical, and optical properties that distinguish them from three-dimensional (3D) materials [9]. These properties are mainly derived from the thin layer structure of atoms, with strong intralayer bonds and weak interlaminar bonds. Their relatively large layer spacings allow for rapid ionic (de)intercalating, while the highly anisotropic 2D structure imparts the ability to transfer charges [10]. At the same time, two-dimensional (2D) materials provide a platform that allows the creation of heterogeneous structures with a variety of properties [11]. Therefore, synthesizing 2D materials containing various components can give us access to a wider range of properties and technical applications. As a newly large family of 2D transition metal carbides, nitrides, and carbonitrides, MXenes have attracted growing focus because of their large and adjustable layer spacing, rich specific surface area, good bending property, high electrical conductivity, hydrophilicity and rich surface functional groups (-F, -OH, -O, etc.) [12,13]. Naturally, since MXene was discovered by Yury Gogotsi's group in 2011 [14], it has been applied in various fields such as sensing, photocatalysis, electrocatalysis, and energy. In terms of energy storage, Gogotsi unfolded the lithium storage activity of MXene through DFT calculations at the beginning of its discovery. Because both Na and K have similar structures and chemical properties to Li, much extensive research has been made on MXene for alkali metal battery applications [15].

To date, many review papers have summarized the advances of MXene in alkali metal-ion batteries [16]. However, MMIBs undergo quite different redox chemistry from alkali metal-ion batteries; hence, the role of MXenes in MMIBs will be different from that in alkali metal-ion batteries. Unfortunately, the study of MXene for MMIBs is still in its infancy, and the compatibility between MXenes and MMIBs is being investigated. Therefore, it is urgent to summarize the latest research progress of functionalized MXene for MMIBs. Herein, this review will first briefly introduce the synthesis and properties of MXene materials. Then, the application of MXenes in MMIBs is categorically overviewed separately in terms of magnesium ion battery, aluminum ion battery, calcium ion battery, and zinc-ion battery. Finally, the advantages, the remained challenges, and the future direction toward the practical applications of MXenes in MMIBs are deeply discussed.

2. MXene

MXene is a class of compounds with a two-dimensional layered structure. Its general formula can be written as $M_{n+1}X_nT_x$, in which M refers to some transition metal elements, such as Sc, Ti, V, Cr, Mo, Hf, Nb, Ta, W, etc. More in-depth studies show that M can be expanded to binary or even multiple metallic elements. X contains the C and/or N element (Figure 1a); T is the surface terminal functional group, generally -F, -OH, -O, etc., which is closely related to the synthesis method [17]. Among them, the early n value is 1~3 [18], and the discovery of $Mo_4VC_4T_x$ extends the scope of research to n = 4 [19]. Later, with the diversification of synthesis mechanisms, the discovery of $Mo_{1.33}CT_x$ [20], $V_{2-x}C$ ($x \leq 0.05$) [21], and solid solution structures [22] greatly enriched the members of the MXene family (Figure 1b).

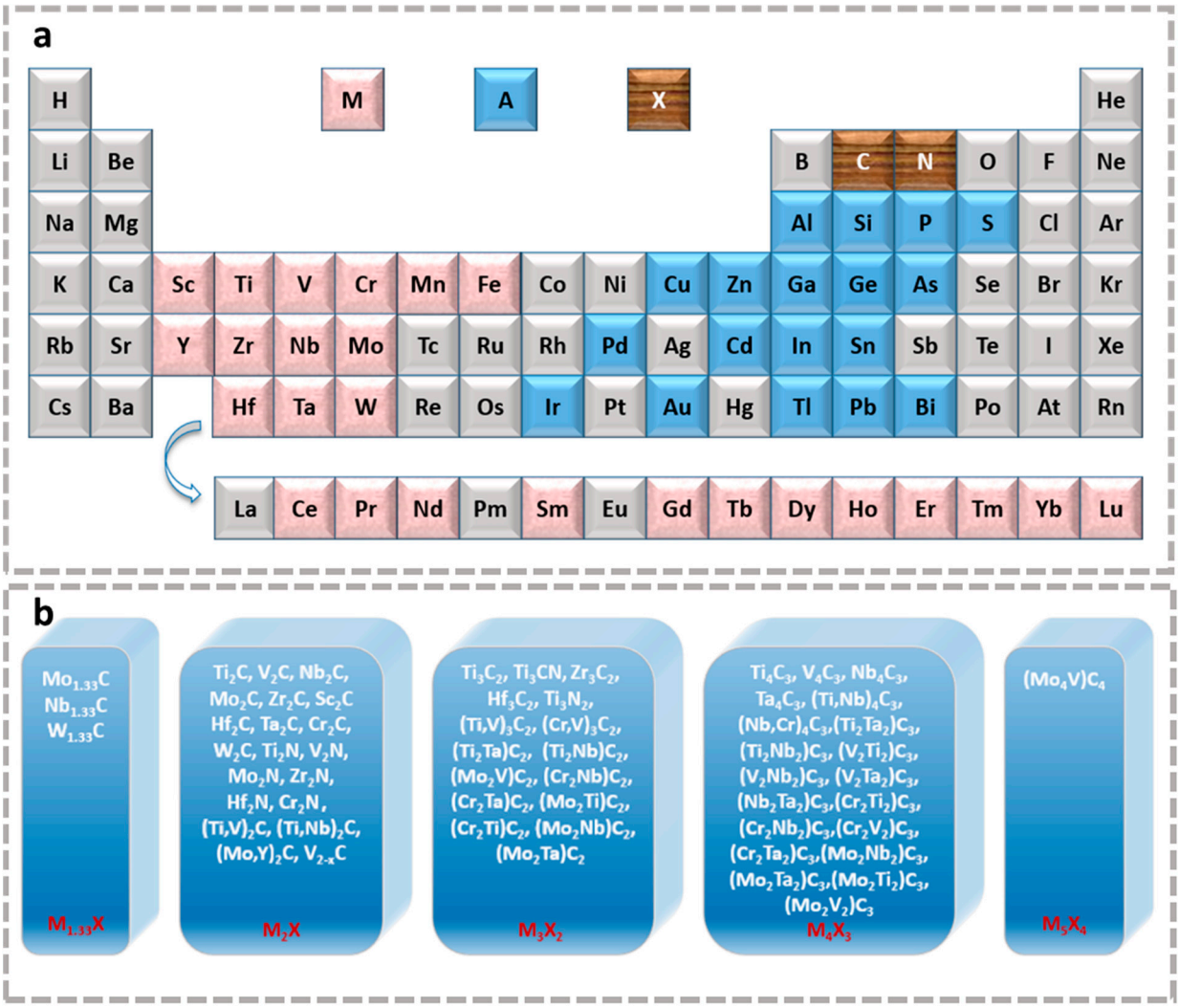

Figure 1. (**a**) Periodic table fragments marked with the "M", "A" and "X" elements in known MAX and MXene phases. (**b**) Currently known MXene compositions, ignoring the terminal here.

2.1. Synthesis of MXene

The most ordinary method for preparing MXene is etching the MAX precursor. MAX [23] can be expressed as $M_{n+1}AX_n$ (*n* ranges from 1 to 4), where M and X are the same compositions as mentioned above; A is mainly from the elements of the main group 13–15, such as Si, Al, Ge, Sn, etc. (Figure 1b). The MAX phase exists as three different types of unit cells with a six-square tightly packed structure of the space group P63/mmc. The A atomic layer in the MAX phase is sandwiched between the densely packed M layers, and the octahedral position is occupied by the X atom. In accordance with the crystal structure of MAX, $M_{n+1}AX_n$ is also recognized with a layered structure, in which the two-dimensional $M_{n+1}X_n$ layer is connected by the A layer. M-A is a metal bond, while M-X has both covalent and ionic bond properties, which are more stable than the M-A bond [24]. This feature makes it possible to remove the A atoms from the MAX phase to obtain MXene.

2.1.1. Fluorine-Containing Etching Method

HF Acid Etching

Unlike the van der Waals forces between black phosphorus [25], the strong metal bonds make directional removal of the A atomic layer still challenging. Until 2011, Gogotsi et al. [14] successfully prepared accordion-like multilayer $Ti_3C_2T_x$ by chemical etching the Al atomic layers in Ti_3AlC_2 with HF acid, which opened the prelude of etching

the A-layer structure from the MAX phase by fluorine-containing etchants (Figure 2a). Thereafter, lots of MXenes have successfully synthesized with different M elements (such as $(V_{0.5}Cr_{0.5})_3C_2$, Nb_2C, V_2C, TiNbC), different X elements (such as Ti_3CN_x) and different compositions (such as Ti_2C, Ta_4C_3) by HF acid etching [18,26], which promotes the universality of HF acid etching in MXene synthesis [14].

Taking the synthesis of Ti_3AlC_2 as an example, the reaction route of HF acid etching is as follows:

$$Ti_3AlC_2 + 3\ HF \rightarrow AlF_3 + 3/2\ H_2 + Ti_3C_2 \quad (1)$$

$$Ti_3C_2 + 2\ H_2O \rightarrow Ti_3C_2(OH)_2 + H_2 \quad (2)$$

$$Ti_3C_2 + 2\ HF \rightarrow Ti_3C_2F_2 + H_2 \quad (3)$$

After the reaction of HF acid with the Al layer, each $M_{n+1}X_n$ group was exposed to two highly active Ti atomic sites, which spontaneously combined with -OH and -F in the solution, so the surface terminal of the HF acid etching method is randomly distributed in -OH and -F groups. As for HF etching, the HF acid concentration, etching time, and etching temperature need to be appropriately adjusted for different precursors [27–29]. Excessive etching time and HF acid concentration will cause defects in the synthesized MXene and even lead to the complete collapse of the structure. Conversely, insufficient etching time or HF acid concentration results in incomplete etching.

In Situ Generation of HF

Although HF acid etching methods are easy to operate and have a wide range of applications, hydrogen fluoride and its aqueous solutions are toxic and harmful. To avoid the use of HF acid, a method of in situ generating HF acids by strong acids (HCl/H_2SO_4) and fluorine-containing salts ($LiF/NaF/KF/CsF/CaF_2$) has emerged. In 2014, Gogotsi et al. [30] successfully prepared $Ti_3C_2T_x$ by etching Ti_3AlC_2 at 40 °C for 45 h with HCl/LiF. Liu et al. [31] etched V_2AlC with NaF/HCl at 90 °C for more than 48 h to obtain V_2C. This synthesis method is milder than HF acid etching, thus greatly reducing the defect content [32]. The prepared MXene is rich in the -F/-OH terminal group, which is easy to form hydrogen bonds, showing hydrophilicity and negative electricity. Due to the spontaneous intercalation of metal cations and H_2O molecules, the prepared MXene exhibits a larger layer spacing and fewer layers than that obtained by the HF acid preparation method, eliminating the subsequent peeling step.

Other Fluoride Salts

In addition to the (in situ) HF acid method, some fluoride salts and their mixtures can also be used for etching purposes to avoid the use of strong acids. Gogotsi et al. [33] prepared Ti_3C_2 by etching 1 M NH_4HF_2 at room temperature, and the embedding of NH_4^+ increased the layer spacing from 18.6 Å to 24.7 Å. Nitride MXene has higher conductivity than carbide, but because of the stronger Al bonding force compared to $Ti_{n+1}AlC_n$ in the $Ti_{n+1}AlN_n$ phase which is soluble in HF solution, the traditional synthesis method is not suitable for nitride MXene. Gogotsi et al. [34] mixed Ti_4AlN_3 powder with molten fluorine salts (59 wt% KF, 29 wt% LiF, 12 wt% NaF) and heated at 550 °C for 30 min under argon gas protection to synthesize $Ti_4N_3T_x$ (Figure 2b), opening up the research field of nitride MXene.

MXene prepared by chemical etching is usually multilayered, it is usually followed by a peeling procedure for better application (Figure 2c). In addition to the metal cation [35] spontaneously interpolated in the etching above, the layer spacing can also be extended by dimethyl sulfoxide (DMSO) [36], tetrabutylammonium hydroxide (TBAOH) [37], isopropylamine [38], tetramethylammonium hydroxide (TMAOH) [39], the water molecule (H_2O), cetyltrimethylammonium bromide (CTAB) [40], etc., and subsequent sonication can mechanically peel off the MXene to form a few-layer suspension.

Although the fluorine-containing etching method can well break the M-A bond to complete the synthesis of a variety of MXene materials, the MXene terminal group etched by the fluorine-containing method is single and the fluoride pollutes the environment,

which is also very harmful to the human body. Therefore, it is urgent to find a feasible fluorine-free etching method to prepare MXene.

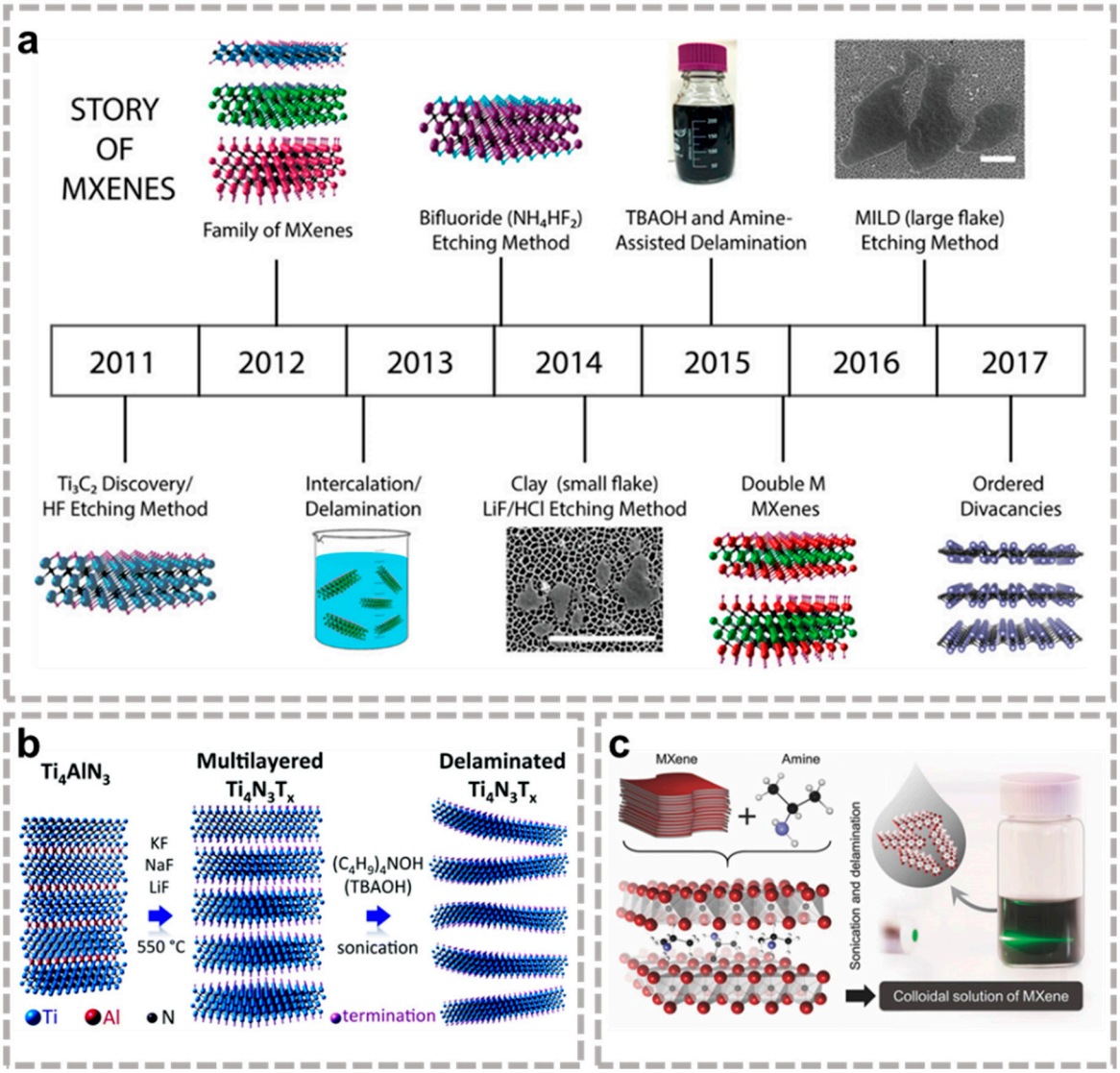

Figure 2. (**a**) The history of MXene synthesis [41]. (**a**) Reproduced with permission from the American Chemical Society. (**b**) Schematic diagram of molten fluorine salt etching $Ti_4N_3T_x$ [34]. (**b**) Reproduced with permission from RSC Pub. (**c**) Nb_2CT_x MXene delamination process [38]. (**c**) Reproduced with permission from WILEY-VCH.

2.1.2. Fluorine-Free Etching Method

Although the fluorine-containing etching method can break the M-A bond to synthesize a variety of MXene materials, the MXene terminal group etched by the fluorine-containing method is single. Therefore, with the amphoteric elements characteristics of Al in the middle of Ti_3AlC_2, Li et al. [42] designed a fluorine-free NaOH-assisted hydrothermal method etching Ti_3AlC_2 to prepare $Ti_3C_2T_x$ (T=OH, O). This method does not produce -F termination groups, but there are special application conditions: (1) alkali concentration and hydrothermal temperature should be screened according to the precursor; (2) Phase A in the original MAX phase needs to be amphoteric/acidic atoms. In 2018, Yang et al. [43] demonstrated a high-efficiency fluorine-free etching method based on Ti_3AlC_2 anodic corrosion in binary aqueous electrolyte (1 M NH_4Cl +0.2 M TMAOH). During this process, NH_4^+ is constantly intercalated to ensure an ongoing reaction, resulting in more than 90% of the single and double layers of MXene. Sun et al. [44] prepared monolayer and few-layer

fluorine-free $Ti_3C_2T_x$ (T=O or OH) by intercalation-alloying-expansion-micro-explosion mechanism. Huang et al. [45] first discovered that Lewis acid molten salts undergo a displacement reaction through redox to produce MXene structures, and Figure 3a shows the etching route using $CuCl_2$ as an example. The capacity of Lewis acids to extract electrons from element A in the MAX phase depends on their respective electrochemical redox potentials in halide fusion. According to thermodynamic calculations (Figure 3b) [46], A atoms in the MAX phase can be engraved by means of molten Lewis acid that has a higher redox potential. Therefore, their group was successful in extending this synthesis strategy to various Lewis acid molten salts ($CuCl_2$, $ZnCl_2$, $FeCl_2$, and AgCl) and more MAX family members with different A elements (Zn, Al, Ga, Si). This method also enables the successful preparation of MXene for specific groups (O, S, Se, Te, Cl, Br, I, NH) [47] by displacement and elimination reactions (Figure 3c,d), extending the boundaries of MAX precursors and providing significant opportunities to tune the surface chemistry of Mxene.

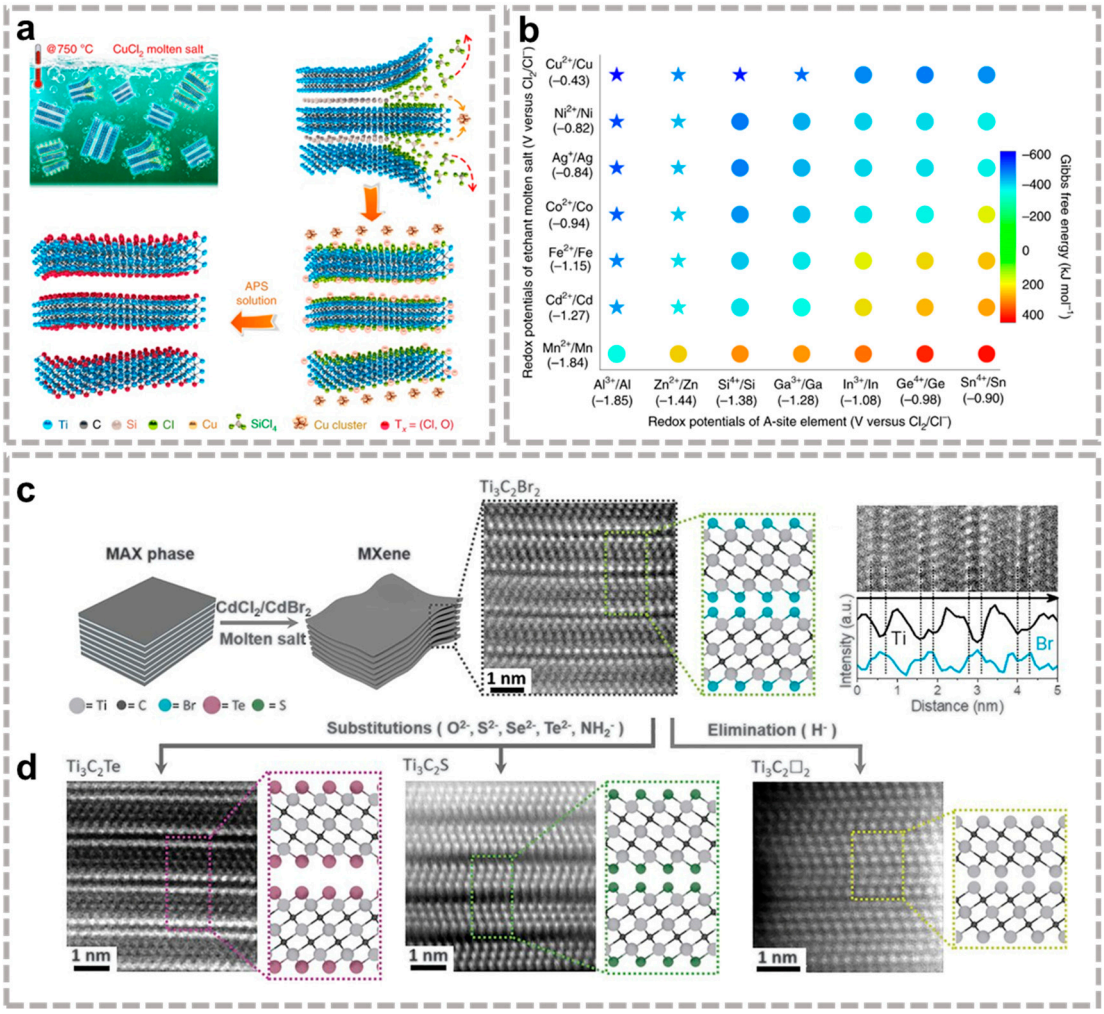

Figure 3. (**a**) Preparation process of $Ti_3C_2T_x$ MXene by reaction between Ti_3SiC_2 and $CuCl_2$; (**b**) Diagram of redox potential and Gibbs free energy (700 °C) [46]. (**a**,**b**) Reproduced with permission from MDPI AG. (**c**) Schematics for etching MAX phases with Lewis acidic molten salts and high-angle annular dark-field (HAADF) image of $Ti_3C_2Br_2$ MXene; (**d**) HAADF diagram of changing the end group by displacement and elimination reactions [47]. (**c**,**d**) Reproduced with permission from AAAS.

2.1.3. Non-Etching Methods

For the method of preparing MXene by means of the etching method, the etching conditions (etchant concentration, temperature, time, etc.) are greatly dependent on the

strength of the M-A bond and *n* value. The prepared MXene is often inevitably defective, and the topography and number of layers are uncontrollable. Dimoulas et al. [48] and Zhao et al. [49] synthesized high-purity bare Mo_2C without terminal groups in one step by means of the chemical vapor deposition method (CVD), which can regulate the size and morphology of materials through synthetic parameters. However, whether other MXene materials can be synthesized through this method is still unknown.

Table 1 summarizes the reagents and surface terminals in different preparation methods of MXene. Through comparison, it is found that although the fluorine-containing etching method has many unavoidable shortcomings, it is still the most popular and widely used etching method. In addition, researchers are also accelerating the research of fluorine-free preparation methods, which not only abandon toxic fluoride reagents but also greatly enrich the surface functional groups of MXene. All in all, each preparation method has its own advantages and disadvantages, so it is necessary to choose the appropriate etching method according to the desired performance of the material.

Table 1. Summary of etching methods.

Etching Method		Surface Terminals	Ref.
Fluorine-containing etching	HF	-F, -OH, -O	[14]
	HCl+LiF/NaF/KF	-F, -OH, -O, -Cl	[30,31]
	NH_4HF_2		[33]
	LiF+NaF+KF	-F, -OH, -O	[34]
Fluorine-free etching	NaOH	-OH, -O	[42]
	Electrochemistry (NH_4Cl+TMAOH)	-OH, -O	[43]
	Intercalation-alloying-expansion-micro-explosion	-OH, -O	[44]
	Lewis acid molten salt	-O, -NH, -S, -Cl, -Se, -Br, -Te	[46,47]
Non-etching method	CVD	/	[48,49]

2.2. Properties of MXene

To select MXene synthesis methods according to the purpose of the experiment, understanding the influence of MXene composition and structure on properties can help us better design experiments.

2.2.1. Structural Stability

Considering the application of a material, including laboratory and industrial applications, the first thing that must be considered is the stability of the material, which is the cornerstone of the performance and application of the material in all aspects. MXene prepared by chemical etching is very similar to its parent MAX. MXene has a hexagonal dense structure in which X atoms are filled as solid solutions to octahedral interstitial sites in the tightly packed structure of M atoms. M_2X-M_2X crystals are typically packed hexagonal stacks with high stability [50]. Rosen et al. [51] experimentally confirmed that Mo_2CT_x has a stable, tightly packed hexagonal structure. In particular, Ti_3C_2 also has a densely packed hexagonal structure, so it is the first to discover and the most studied MXene material. The M_4X_3-M_4X_3 structure and the M_3X_2-M_3X_2 structure are typical face-centered cubic crystal structures, making these two materials unstable [52]. This structure can be stabilized by introducing another transition metal element, M′ (such as Ti) [53].

2.2.2. Environmental Stability

The bare MXene surface has abundant reactive sites and excellent conductivity due to the presence of transition metal-free electrons, but this also brings challenges to the long-term stable existence of MXene in the environment. Zhang et al. [54] exposed the $Ti_3C_2T_x$ colloidal solution to air, which was completely oxidized to TiO_2 in 30 days. The stability of MXene materials under water and oxygen conditions is a key factor restricting their development, and the introduction of surface terminals, surface modification, or the construction of MXene composites to occupy the active site can effectively slow down

the oxidation rate and improve the stability of MXene. For example, in $Ti_3C_2T_x$, the -O-containing MXene is more stable than the -F/-OH containing group [55].

2.2.3. Interlayer Stability

In MXene, the layers rely on the van der Waals force between -F/-O and the hydrogen bonds between -F/-O and -OH to link, and the strength of the hydrogen bonds between layers is determined by the number and distribution of -OH and -F/-O on the sheet [56]. The weak interlayer adhesion is conducive to peeling by various intercalators. However, it generates stack tendency due to its large surface energy, leading to hydrophilicity and conductivity attenuation in the practical application. Currently, stacking between layers can be avoided by increasing layer spacing, building three-dimensional (3D) network structures, or building composite materials. Layer spacing is influenced by a combination of surface termination, synthesis method, precursor, *n* value, and intercalator. The originator of MXene [14] proposed that the geometric optimization of hydroxylated and fluorinated structures led to the expansion of the original Ti_3AlC_2 lattice by 5% and 16%, respectively. Conversely, simply removing the Al atom without being replaced by a functional group would result in a 19% contraction of the structure. Therefore, the presence of surface terminals will occupy the exposed Ti atomic active site, increasing the stability of the material. At the same time, the tendency to stack can be suppressed by reducing the surface contact with the material. The vacuum filtration step of MXene during preparation is subjected to atmospheric pressure, resulting in reduced layer spacing and increased stacking. Starting from the material synthesis method, Xu et al. [57] replaced vacuum filtration with natural sedimentation, and the prepared layer spacing changed from the original 14.06 Å to 14.76 Å, showing good stability (Figure 4e). In addition, the layer spacing of MXene materials can also be adjusted by intercalation reaction or by regulating the precursor MAX phase. Typical intercalators have been described in the previous synthesis section and will not be repeated here. Zhou et al. [58] also obtained an increased layer spacing by etching the precursor V_4AlC_3 after ball milling (c value changed from 2.534 to 3.210 nm, Figure 4f). At the same time, some researchers have shown that for the same type of MXene, the larger the *n* value, the larger the layer spacing [5]. The increased layer spacing not only contributes to the stability of MXene materials but also exposes more active sites, broadens ion transport channels, and further activates more potential of MXene.

The construction of a three-dimensional network structure can effectively avoid stacking between layers and build an ion transport network, so as to better utilize the high conductivity of MXene material, and also has a miraculous effect in alleviating some high-volume strain materials. The template method and freeze-drying method are common methods for constructing 3D network structures. Xu et al. [59] in situ grew S particles on the surface of Ti_3C_2 by chemical reduction, after which the S particles were removed as templates at a high temperature of 300 °C to obtain flexible MXene foam with a well-developed 3D structure (Figure 4g). Gogotsi and colleagues [60] prepared porous Ti_3C_2 (p-Ti_3C_2) by rapid and simple chemical etching using in situ oxidation TiO_2 as a template at room temperature (Figure 4h), which is used as an electrode material for lithium-ion batteries with long lifetime and excellent rate performance (330 mAh g^{-1} at 10 C). Yang et al. [61] freeze-dried the $Ti_3C_2T_x$/CNT nanosheet colloidal solution, the specific procedure is illustrated in Figure 4a, and the SEM of the resulting parallel arrangement of $Ti_3C_2T_x$/CNT (PA-MXene/CNT) structure is depicted in Figure 4b–d. It can be seen that numerous pores are formed between the nanosheets, avoiding the stacking of $Ti_3C_2T_x$ nanosheets. Because of the large specific surface area and rich active sites of MXene, it is easy to connect with many electronic active materials by ultrasound, hydrothermal and other methods. The introduction of composite materials is often accompanied by an increase in layer spacing, and they can also be seen as special intercalators in this regard. Specific applications are presented in "Applications in Multivalent Metal-Ion Batteries (MMIBs)".

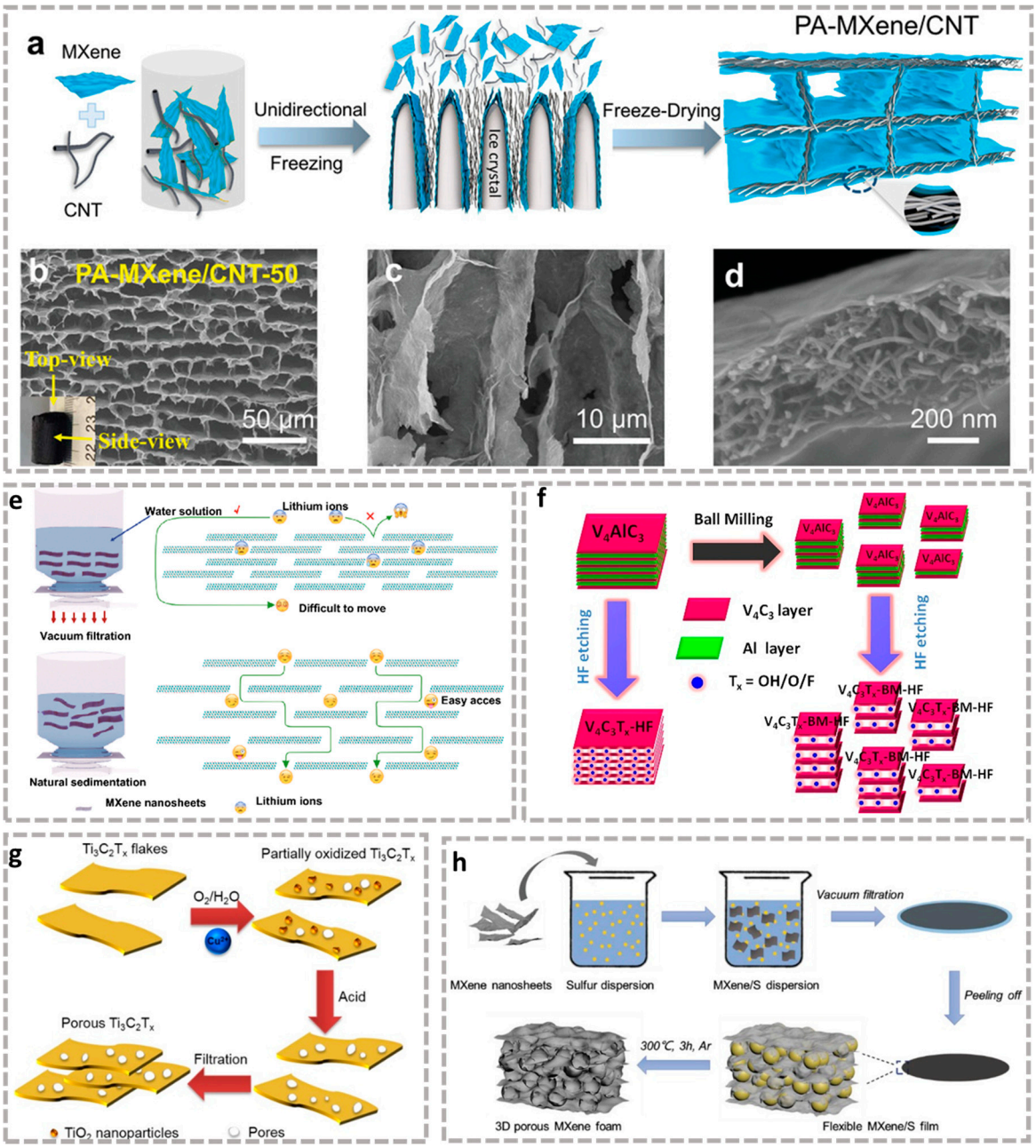

Figure 4. (**a**) PA-MXene/CNT preparation scheme using unidirectional freeze-drying; (**b**–**d**) SEM image of PA-MXene/CNT [61]. (**a**–**d**) Reproduced with permission from WILEY-VCH. (**e**) Comparison of MXene films naturally sedimented and conventional filtered under vacuum [57]. (**e**) Reproduced with permission from Springer Nature. (**f**) Schematic showing the two different processes of $V_4C_3T_x$ MXene [58]. (**f**) Reproduced with permission from ELSEVIER BV. (**g**) Diagram showing the chemical engraving of $Ti_3C_2T_x$ flakes to produce a porous structure [60]. (**g**) Reproduced with permission from John Wiley and Sons. (**h**) Diagram of the porous, free-standing, and flexible 3D MXene foam prepared with an S template [59]. (**h**) Reproduced with permission from WILEY VCH.

2.2.4. Mechanical Properties

MXene inevitably carries terminal groups T_x (-F, -OH, -O) during synthesis, which is conducive to stabilizing bare MXene materials. It can also avoid the collapse of the atomic layer on the surface of bare MXene materials due to tensile strain, improving the mechanical flexibility of materials [62]. It is therefore urgent to examine the impact of terminal groups on performance. Many studies have found that the terminal group greatly

reduces the elastic coefficient of intrinsic MXene [63,64], but the elastic coefficient is still higher than the original MAX phase and other two-dimensional materials (such as MoS_2) excluding graphene [65]. The elastic coefficient relationship of typical terminal groups is -O > -F > -OH, which is proved by nanoindentation experiments to measure Young's modulus of $Ti_3C_2T_x$ [66]. In addition, the presence of surface terminal groups can also greatly enhance the bending properties of MXene, making MXene materials show great application prospects in composite structures and flexible electronics.

2.2.5. Electronic Performance

The introduction of surface terminals can improve MXene stability but may come with a certain sacrifice in electronic performance (Figure 5). Theoretical calculations suggest that bare MXene exhibits metallic properties [67], although most bare MXenes have not been experimentally synthesized. The introduction of terminal groups turns MXene into a semiconductor or even a topological insulator. DFT calculations show that most M_2CT_x compounds with functional groups on their surfaces are semiconductors with bandgap values that typically increment according to the atomic number of "M" and with the order of -O > -F > -OH with the terminal group [68,69]. For example, after converting Sc_2CT_2 (T=F, OH, O), Ti_2CO_2, Zr_2CO_2, and Hf_2CO_2 into semiconductors, the band gap of Sc_2CT_2 (T=F, OH, O) is 1.03, 0.45 and 1.8 eV, respectively, and the band gap values of Ti_2CO_2, Zr_2CO_2, and Hf_2CO_2 are 0.24 eV, 0.88 eV, and 1.0 eV, respectively [70]. Further, electronic performance is also related to M and X types. "M" is Cr, W, and Mo, which may be topological insulators [71], while Ti_3C_2, Ti_4C_3, V_2C, and Nb_4C_3 maintain metallic properties [72]. It was also found that nitride and carbonitride MXenes have higher metallicity than carbide MXene due to the fact that nitrogen has more electrons [73].

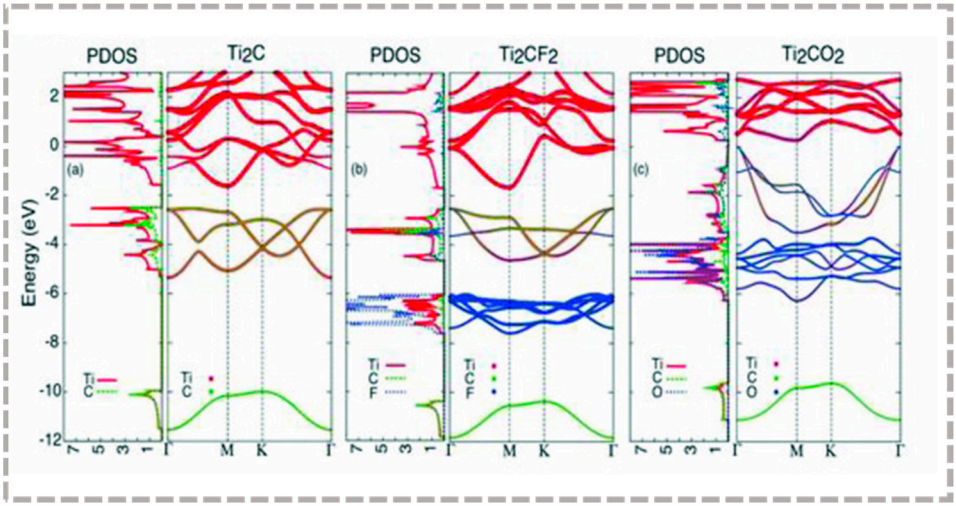

Figure 5. Band structure diagram of the -OH, -F terminations and bare Ti_2C MXene monolayers, showing that MXene changes from metal to semiconductor due to changes in surface chemistry [70]. Reproduced with permission from WILEY VCH.

In addition to theoretical studies, there are also studies that measure the resistivity of some MXenes experimentally. We summarize the results in Table 2. It can be seen that the sheet resistance of some MXenes is in the same order of magnitude as graphene, reflecting excellent conductivity.

Table 2. Resistivity of some MXenes and graphene.

Name	Sheet Resistance, Ω sq−1	Resistivity, Ω m	Ref.
Ti_2C	339	0.068	
TiNbC	171	0.052	
Ti_3CN_x	125	0.037	[18]
Ta_4C_3	104	0.021	
Ti_3C_2	22	0.005	
$Mo_{1.33}C$	/	0.033	[20]
Mo_2C	/	0.6	
graphene	350	/	[74]

2.2.6. Surface Terminals

In addition to affecting the stability of MXene materials, surface terminals of special groups have some specific uses. The capacity of the -O terminal is significantly higher than that of -F/-OH in energy storage performance [75]. -S terminal has an adsorption effect on dissolved polysulfides and the cycling performance of the battery can be obvious when used in Li-S batteries [76]. The tunable fit of surface terminal groups begins in the material synthesis phase. When etching using fluorine-containing methods, the terminals are mainly -O, -OH, and -F [77]. -F content also depends on the type of etchant used. For example, the HF acid etching -F terminal is four times LiF+HCl [77]. Fully chlorinated MXene (T=Cl) is obtained using $ZnCl_2$ etching [46]. Secondly, the MXene terminal group can also be changed by post-treatment such as displacement reaction, annealing treatment, chemical method, or reaction with alkali metal hydroxide. Kamysbayev et al. [47] successfully prepared $Ti_3C_2T_x$ containing S, Se, Te, Cl, Br, and NH terminals by displacement reaction, and a variety of groups brought different stability and electronic properties from traditional -F/-O/-OH. However, the discovery time of these groups is short, so the current research on their performance is not in-depth enough. Persson et al. [78] completed the transition from -F to -O by thermal annealing at 750 °C, and Xie et al. [55] completed the transition from -OH to -O. Although the -O band gap is slightly higher than -F, the stability of the -O-terminal group is greatly improved, and it has been proven to have the highest storage capacity, so the O-terminal group may be advantageous in energy storage batteries. The post-treatment method also expands the scope of the application of fluorine-containing etching.

However, MXene also has some challenges. As we mentioned earlier, The M_4X_3-M_4X_3 structure and the M_3X_2-M_3X_2 belong to unstable face-centered cubic structures. However, some of these structures MXene exist (Zr_3C_2, Hf_3C_2, V_4C_3, Nb_4C_3, Ta_4C_3), while others do not exist with this chemical formula at all (V_3C_2, Mo_3C_2, Cr_3C_2, Mo_4C_3, Cr_4C_3). In addition, M_2C-M_2C MXene is more active than other types and is susceptible to environmental oxidation. The stability of N-based MXene is lower than its carbide counterpart. Therefore, when using M_2C-M_2C or N-based MXene, strict oxidation resistance or rational utilization of oxidation is necessary.

Therefore, choosing the right MXene and appropriate etching method is primarily for the experiment. If used as battery electrode materials, Ti_3C_2, V_2C, Nb_2C, etc. with good conductivity are preferred. Once the type and number of layers are determined, MXene is more of a surface chemical. Terminal groups can improve the stability of the material, improve layer spacing, and affect electronic and mechanical properties. The modification of the terminal group by the post-treatment method widens the access channels of the individual terminals. In addition, the trend of MXene being stackable can be improved by many treatments, offering more potential for MXene applications in the energy storage area [79].

3. Applications in Multivalent Metal-Ion Batteries (MMIBs)

The MMIBs currently studied mainly include Mg^{2+}, Al^{3+}, Ca^{2+}, and Zn^{2+} batteries. Because of their abundant reserves and significantly lower vivacity than lithium, the corresponding metal is commonly used as an anode in MMIBs [80–82]. However, due

to the high charge and large hydration radius of polyvalent ions, the ion has a strong binding force with electronic materials and slow diffusion kinetics, which is not conducive to the reversibility of the battery [83]. Therefore, new challenges are posed to the electrode materials of MMIBs.

3.1. Magnesium Ion Batteries (MIBs)

Magnesium [84] is a reactive metal with a density of 1.74 g cm^{-3}, a high theoretical volumetric energy density (~3833 mAh cm^{-3}), rich reserves, low price (1/24 of Li), good thermal and electrical conductivity, and low potential (Mg^{2+}/Mg redox potential −2.37 V). In the periodic table, magnesium is diagonal to lithium and has similar chemical properties. Therefore, the research of MIBs as an alternative to lithium-ion batteries is of great significance for the exploration and utilization of future energy.

However, MIBs lack suitable cathode materials with high ion diffusion/intercalation rates [85] hindered by the common problems of polyvalent ions. It is expected that MXene will store magnesium because of its wide and adjustable layer spacing, high conductivity, and abundant surfactant sites. Based on theoretical calculations, Ti_2CO_2 has a theoretical magnesium storage capacity of 570 mAh g^{-1} (comparable to the alloy anode) [55], demonstrating the magnesium storage activity of MXene material. Xie et al. [55] calculated the reaction mechanism of Mg^{2+} in MXene materials. When MXene is used as a cathode material for MIBs, Mg^{2+} will first be adsorbed to negatively charged O-MXene through electrostatic interaction due to negative surface adsorption energy. Herein, because of the positive adsorption energy of OH-MXene and the instability of F-MXene, these two are not considered. Because of the small repulsion of Mg^{2+} and the transition metal atoms in MXene and the strong shielding of negative electron clouds, Mg^{2+} is the only polyvalent metal ion that can form two intact adsorption layers. After that, the lower adsorbed Mg^{2+} is intercalated/deintercalated between the MXene layers as the reaction progressed, and the upper adsorbed Mg^{2+} is released/stored by similar deposition/dissolution mechanisms, which greatly increases the magnesium storage capacity of MXene. It is worth noting that Mg^{2+} on the adsorption layer does not form a passivation layer like magnesium metal during deposition, which is conducive to the reaction. Finally, in the presence of Mg, O-MXene undergoes a transformation reaction to decompose into bare MXene and magnesium oxide. Although the ion diffusion of bare MXene is better than that of O-MXene, in fact, due to the lack of support of stable electrolyte, the final conversion reaction has not been experimentally demonstrated, and even the dissolution/deposition reaction of the second adsorption layer does not necessarily occur. It is inevitable that the prepared MXene material contains terminals, and the polyvalent metal-ion diffusion performance in T_x-MXene is far inferior to that of alkali metal ions, which make the rate of performance slightly worse. Therefore, promoting Mg^{2+} intercalation/deintercalation by improving the adsorption and diffusion processes is a key driver for enhancing the utilization of MXene materials.

Xu et al. [40] demonstrated the ability of CTAB intercalated $Ti_3C_2T_x$ ($Ti_3C_2T_x$/CTAB) for the storage of magnesium ions, whereas the original $Ti_3C_2T_x$ did not function well (Figure 6a). The main performance improvement factor is the reduction of the diffusion barrier of Mg^{2+} on the surface of $Ti_3C_2T_x$/CTAB (about 0.19 eV, Figure 6c–h), which endows the prepared $Ti_3C_2T_x$/CTAB cathode an elevated capacity of 300 mAh cm^{-3} at 50 mA g^{-1} (Figure 6b). Additionally, the intercalation of CTAB prevents $Ti_3C_2T_x$ from self-stacking, improving the overall stability. Besides that, the pre-intercalated layers of Mg^{2+} [86], K^+ [87], and nanocarbon materials [88] can also realize the magnesium storage properties of MXene materials.

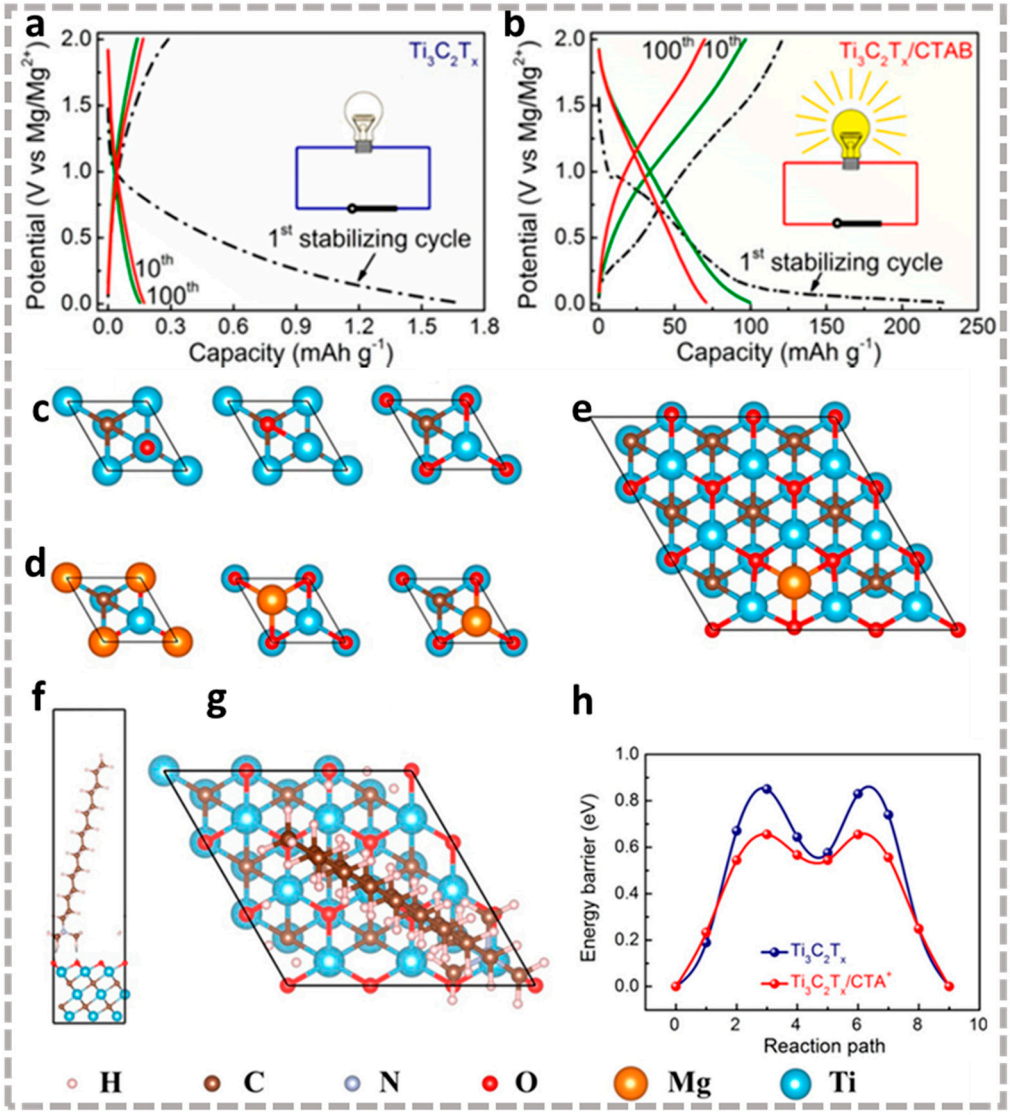

Figure 6. Galvanostatic charge/discharge (GCD) curves of (**a**) $Ti_3C_2T_x$ and (**b**) $Ti_3C_2T_x$/CTAB electrode at different cycles at 0.05 A g^{-1}; Top view of the structures for (**c**) an O atom and (**d**) a Mg atom adsorbed on 1 × 1 Ti_3C_2 surface at the top site, body-centered cubic (bcc) site, and face-centered cubic (fcc) site, respectively. Top view of (**e**) Mg^{2+} and (**g**) CTA^+ as well as (**f**) side view of CTA^+ adsorbed on the 3 × 3 Ti_3C_2O surface; (**h**) Diffusion profile of Mg^{2+} on Ti_3C_2O and CTA^+/Ti_3C_2O surface in nudged elastic band calculations [40]. Reproduced with permission from ACS Nano.

Apart from being directly used as an active electrode material, MXene is an excellent substrate material due to its good laminated structure and electrical conductivity. The combination with magnesium cathode active material can stimulate the maximum potential for both of them. As a typical magnesium storage cathode material, MoS_2 is plagued by low capacity and poor cycle stability. Xu et al. [89] introduced $Ti_3C_2T_x$ as an "enhancer" into MoS_2 by in situ hydrothermal method to prepare the $MoS_2/Ti_3C_2T_x$ composite structure. MXene adsorbed Mo^{4+} as a nucleation site, and the flaky MoS_2 gradually grew to obtain thin petal-like $MoS_2/Ti_3C_2T_x$ (Figure 7a–d). This particular topography provides more exposed active sites for Mg^{2+} storage while providing more channels for improving Mg^{2+} diffusion kinetics. In addition, MXene's excellent electrical conductivity gives the composite excellent electron transport properties. At the same time, MoS_2 between MXene layers further inhibits the stacking of MXene materials, and the confinement effect of MXene structure synergistically alleviates the volume expansion during cycling, jointly maintaining

the stability of the composite material. For these reasons, $MoS_2/Ti_3C_2T_x$ composite reached a reinforced capacity of 165 mAh g^{-1} at 50 mA g^{-1}, which was much higher than other MoS_2 (Figure 7e,f). Li et al. [90] synthesized TiS_2/Ti_3C_2 composites by hydrothermal assembly using Ti_3C_2 MXene as an ideal substrate. Compared with pure TiS_2 cathode material, TiS_2/Ti_3C_2 has a cumulative capacity of 97 mAh g^{-1} for MIBs at 50 mA g^{-1}. Liu et al. [91] prepared $Ti_3C_2/CoSe_2$ heterojunctions by in situ growth of MOF(ZIF-67) structure on Ti_3C_2 combined with selenization (Figure 7g). Similar to the mechanism proposed by Xu et al. [89], $Ti_3C_2/CoSe_2$ as a cathode material for MIBs showed excellent cycle life (>500 cycles) and excellent rate performance (75.7 mA h g^{-1} at 1000 mA g^{-1}, Figure 7h,i). During the in situ process, MXene is more susceptible to interference from external unstable factors (such as high temperature) to accelerate the oxidation process. Zhu et al. [92] prepared $VS_4@Ti_3C_2/C$ by adding glucose to inhibit the oxidation of Ti_3C_2 by providing a reducing environment with the in situ synthetic of $VS_4@Ti_3C_2$. Glucose is anchored on the surface of Ti_3C_2 by forming a hydrogen bond with the oxygen-containing terminal, and finally forms a carbon film uniformly coated on the surface of Ti_3C_2 through pyrolysis, which not only achieves the purpose of inhibiting oxidation but also increases the overall conductivity of the system. $VS_4@Ti_3C_2/C$ as a cathode has a smaller impedance than VS_4, showing a capacity of 492 mAh g^{-1} at 50 mA g^{-1}, as well as over 900 cycles stability and excellent rate performance. Nevertheless, the in situ generation method is highly susceptible to oxidation of MXene, so the development of simpler composite combination methods is also a favorable solution. Yang et al. [93] prepared $Li_4Ti_5O_{12}$ nanosheets/d-Ti_3C_2 flexible film(LTO NSs@d-Ti_3C_2) by simple ultrasonic mixed filtration, which perfectly utilized the excellent kinetic properties, abundant active sites, and mutually supportive stability provided by the composite structure to achieve a self-supporting and non-current collecting flexible electrode.

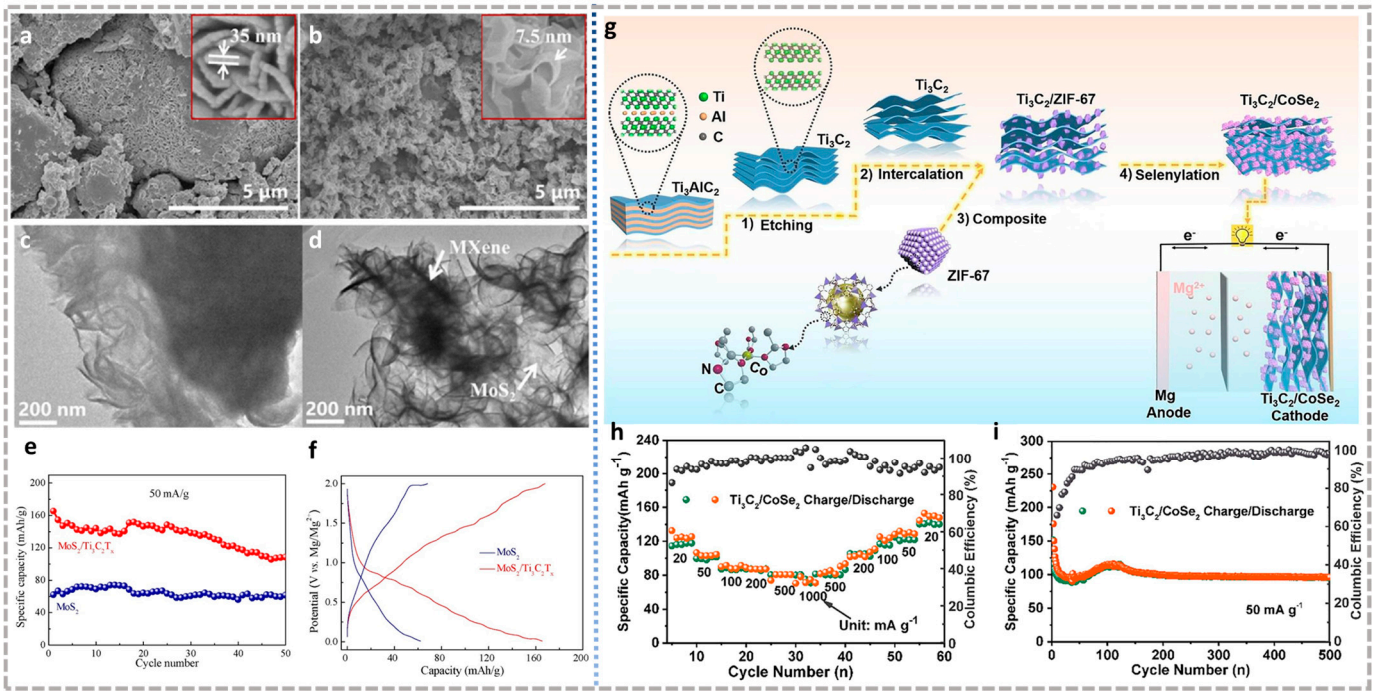

Figure 7. FESEM and TEM images of (**a**,**b**) MoS_2 and (**c**,**d**) $MoS_2/Ti_3C_2T_x$ composite. The illustrations show the corresponding image with different magnifications. (**e**) Cycle performance and (**f**) charge/discharge curves of MoS_2 and $MoS_2/Ti_3C_2T_x$ electrodes in MIBs after stabilization [89]. (**a**–**f**) Reproduced with permission from Elsevier. (**g**) Schematic illustration of the $Ti_3C_2/CoSe_2$ synthesis process and half-cell mechanism. (**h**) Rate capability at different current densities and (**i**) cycling performance at 50 mAg^{-1} of $Ti_3C_2/CoSe_2$ [91]. (**g**–**i**) Reproduced with permission from Elsevier BV.

In composite materials, the proportion between the constituents is vital. Too little MXene leads to excessive filling between MXene layers, which has a negative impact on ion transport; too much MXene challenges the uniformity of combinations. Li et al. [94] demonstrated that in MnO_2/V_2C composites with MnO_2 content of 20%, MnO_2 and V_2C achieve complementary advantages, where the uniform combinations facilitate the mobility of ions. Therefore, for the composite of different materials with MXene, the first thing to prove is the feasibility of compounding, in other words, to consider the stability after compounding. Followed immediately, the optimal compound ratio needed to be determined according to the actual situation.

It can be found that the preparation of MXene composites is an important part of MXene applications. Therefore, here is a brief summary of composite synthesis methods. In addition to the in situ generation method similar to $MoS_2/Ti_3C_2T_x$ [89], in situ conversion (partial oxidation [95], vulcanization [96] or selenization [97]) and ex situ methods (electrostatic action or van der Waals self-assembly by ball milling [98], ultrasound [93], spray [99,100], chemical vapor deposition [101], etc.) can also successfully prepare MXene composites.

In order to increase MXene's magnesium storage capacity, the researchers also turned to magnesium-lithium hybrid batteries (HMLBs). In such batteries, the cathode material needs to have good dual-ion (Mg^{2+} and Li^+) compatibility. The storability of MXene to single ions (Li^+, Mg^{2+}), respectively, makes it a favorable candidate for HMLB electrode materials. Gogotsi et al. [102] report a free-standing flexible $Ti_3C_2T_x$/carbon nanotube ($Ti_3C_2T_x$/CNT) composite "paper" HMLB electrode that provides only 105 mAh g^{-1} reversible capacity at 10 mA g^{-1}. Therefore, the researchers hope to increase the layer spacing by selecting other intercalators or compounding some "pillar effect" materials to achieve high-capacity HMLBs. Prelithiated-V_2C [103] as a cathode can achieve a fascinating reversible capacity of about 230 mA h g^{-1} at a current density of 0.02 A g^{-1}. The increased interlayer spacing influenced by Li^+ pre-embedding unlocked additional ion diffusion channels, which provides insight into the rapid reaction kinetics and high Mg^{2+} storage capacity of MXene. Similarly, Li et al. [104] obtained $Ti_3C_2T_x$ with different layer spacing through different alkyl chain surfactant intercalation layers, indicating that Mg^{2+} intercalating/de-intercalating is only possible if the layer spacing is greater than 1.83 nm. They also pointed out that the N element in the CTAB is tightly bound to $Ti_3C_2T_x$, which can be regarded as N doping, further neutralizing the electronegativity of $Ti_3C_2T_x$ so that Ti_3C_2/CTAB exhibits a reversible capacity of 115.9 mA h g^{-1} at 0.1 A g^{-1} in an HMLB. This method has also been experimentally proven to be applied to Mo_2C MXene [102].

At present, the application of MXene in MIBs mainly focuses on the cathode. The biggest challenge of MXene when storing Mg^{2+} independently is the slow Mg^{2+} diffusion, so various intercalation methods are often used to improve MXene's Mg^{2+} storage performance, which is also reflected in HMLBs. Some studies on transition metal chalcogenides as cathodes for MIBs have been added to Table 3. Compared with other cathode materials, the magnesium storage capacity of $Ti_3C_2T_x$/CTAB can be compared with some classical MIBs cathode materials (50 mAh g^{-1} for V_2O_5 [105], 130 mAh g^{-1} for Mo_6S_8 [106], 85 mAh g^{-1} for MnO_2 [107]). In composites, with the addition of MXene-Ti_3C_2, the storage capacity of magnesium ions of MoS_2 and TiS_2 is improved. MXene-Ti_3C_2 nanosheets with good electrical conductivity provide a looser structure and more active sites for the entry and exit of magnesium ions. Of course, intercalation and composite can cooperate to achieve a win-win situation, so we briefly summarize some composite synthesis methods above.

3.2. Aluminum Ion Batteries (AIBs)

Aluminum [108] is the most abundant metal element in Earth's crust. The specific volume capacity of aluminum metal is 8046 mAh cm^{-3}, which is up to four times that of lithium metal, and its mass-specific capacity is 2980 mAh g^{-1}, which is also relatively high. In addition, the low cost and environmental friendliness advantages of AIBs further promote its research progress. However, the stable cycle of Al^{3+} is closely related to the electrolyte. It was found that only the ionic electrolyte (anhydrous aluminum

chloride ($AlCl_3$) + 1-ethyl-3-methylimidazolium chloride ([EMIm]Cl)) can ensure the dissolution/deposition of the aluminum metal anode, in which the carriers exist in the form of $AlCl_4^-$ or $Al_2Cl_7^-$ [109]. Therefore, the main research is divided into two categories: one focuses on AIBs where Al^{3+} is extracted from cathode materials, and the other focuses on the two-ion reaction of $AlCl_4^-$ or $Al_2Cl_7^-$ as carriers at the cathode. At present, the transition metal chalcogenides (TMCs) are mainly used as cathode materials for AIBs, but their extraction process of Al^{3+} is the result of the combined action of intercalation and phase transition, thus resulting in poor cycle stability [110]. This is because of the difficulty of extracting Al^{3+} from the electrolyte and the strong interaction between Al^{3+} and the electrode material that the performance of AIBs cathode materials still needs to be further improved.

Similar to the storage mechanism of Mg^{2+} in MXene, the adsorption energy of Al^{3+} on O-MXene is slightly higher than that of Mg^{2+} because of the strong repulsion between Al^{3+} and the transition metal atoms. As a result, during the adsorption process, the adsorption layer only has a 2/3 coverage, so the intercalation/deintercalation storage mechanism of Al^{3+} is revealed [55]. However, thanks to the charge contribution of each atom (1.09 e^-/Al, higher than 0.76 e^-/Mg, 0.79 e^-/Ca), MXene still has a high aluminum storage capacity. For instance, theoretical calculations show that Ti_2CO_2 has a theoretical aluminum storage capacity of 552 mAh g^{-1} [55].

Beidaghi et al. [111] confirmed that Al^{3+} can be reversibly inserted into the V_2CT_x host. With the help of TBAOH, the expanded layer spacing improved electrochemical performance (Figure 8a,b). The optimized MXene provides a high capacity of over 300 mAh g^{-1} at of 100 mA g^{-1}, along with an approximately 50% capacity remaining after 100 cycles at 200 mA g^{-1} (Figure 8c–e). The embedding mechanism is revealed as follows: during the discharge process, Al^{3+} generated by dissociation of $Al_2Cl_7^-$ at the electrode/electrolyte interface is inserted into the MXene interlaminar region. At the same time, the anode undergoes the process of Al^{3+} generated by Al dissolution contacting $AlCl_4^-$ to form $Al_2Cl_7^-$. The charging process is the opposite. Although continuous capacity deterioration was observed, the specific capacity and cycling performance reported here were the best at that time. With the deepening of the research of AIBs, Lee et al. [112] found that the Fe_2CS_2 obtained by replacing Ti with a late transition metal Fe and replacing O-terminal groups with S-terminal groups has higher capacity and kinetic properties than Ti_2CO_2. This is attributed to the redistribution of charge under the action of Fe and -S, along with the reduction of the Al^{3+} intercalation barrier by -S.

Recently, Li et al. [113] found that Ti_3C_2 possesses a 455.5 mAh g^{-1} capacity at 100 mA g^{-1} when used as a cathode in AIBs, but the stability is extremely poor due to the adsorption of polychloride anions by the -OH and -F terminals. Therefore, they improve the performance by building composite materials. They first ultrasonicated the mixture of CTAB and Ti_3C_2 to enlarge the layer spacing in Ti_3C_2 (Ti_3C_2@CTAB). Then, after being selenized, selenium was deposited between layers to prepare Ti_3C_2@CTAB-Se [113]. Through the intercalation of CTAB and selenium, Ti_3C_2@CTAB-Se electrode demonstrates 583.7 mAh g^{-1} discharge capacity at 100 mA g^{-1}, and still 132.6 mAh g^{-1} maintained after 400 cycles. It is worth noting that this cathode composite relies on $AlCl_4^-$ to achieve charge storage/release, in which selenium can not only improve the surface adsorption of $AlCl_4^-$ but also improve the overall capacity as an active material. Li et al. [114] synthesized D-$Ti_3C_2T_x$@S@TiO_2 with -S terminal by in situ deposition S into the DMSO stripped $Ti_3C_2T_x$ layers and then high-temperature oxidation method (Figure 8f), whose working mechanism is also $AlCl_4^-$ intercalation/deintercalation when used as the cathode of AIBs (Figure 8g). Unlike in the previous study, the residual S between the layers will form polysulfides dissolved in the electrolyte during the electrochemical activation process at a small current density and are not used as active materials. The D-$Ti_3C_2T_x$@S@TiO_2 shows a discharge capacity of 151.3 mAh g^{-1} after 120 cycles (72.3% retention), which is about 80.0 mAh g^{-1} higher than $Ti_3C_2T_x$ in AIBs (Figure 8h). The improvement is mainly due to the following reasons: the -S terminal generated by high temperatures avoids the capacity

decay caused by the irreversible reaction of -OH and $AlCl_4^-$, and the TiO_2 generated by partial oxidation attached to the surface to maintain the overall frame to further increase the stability of MXene material. It can be seen that scientists have noticed the exploration of MXene in AIBs. However, both bare and modified MXene have the problem of rapid deterioration of capacity, and the mechanism needs to be further explained to better guide the design of cathode materials for AIBs.

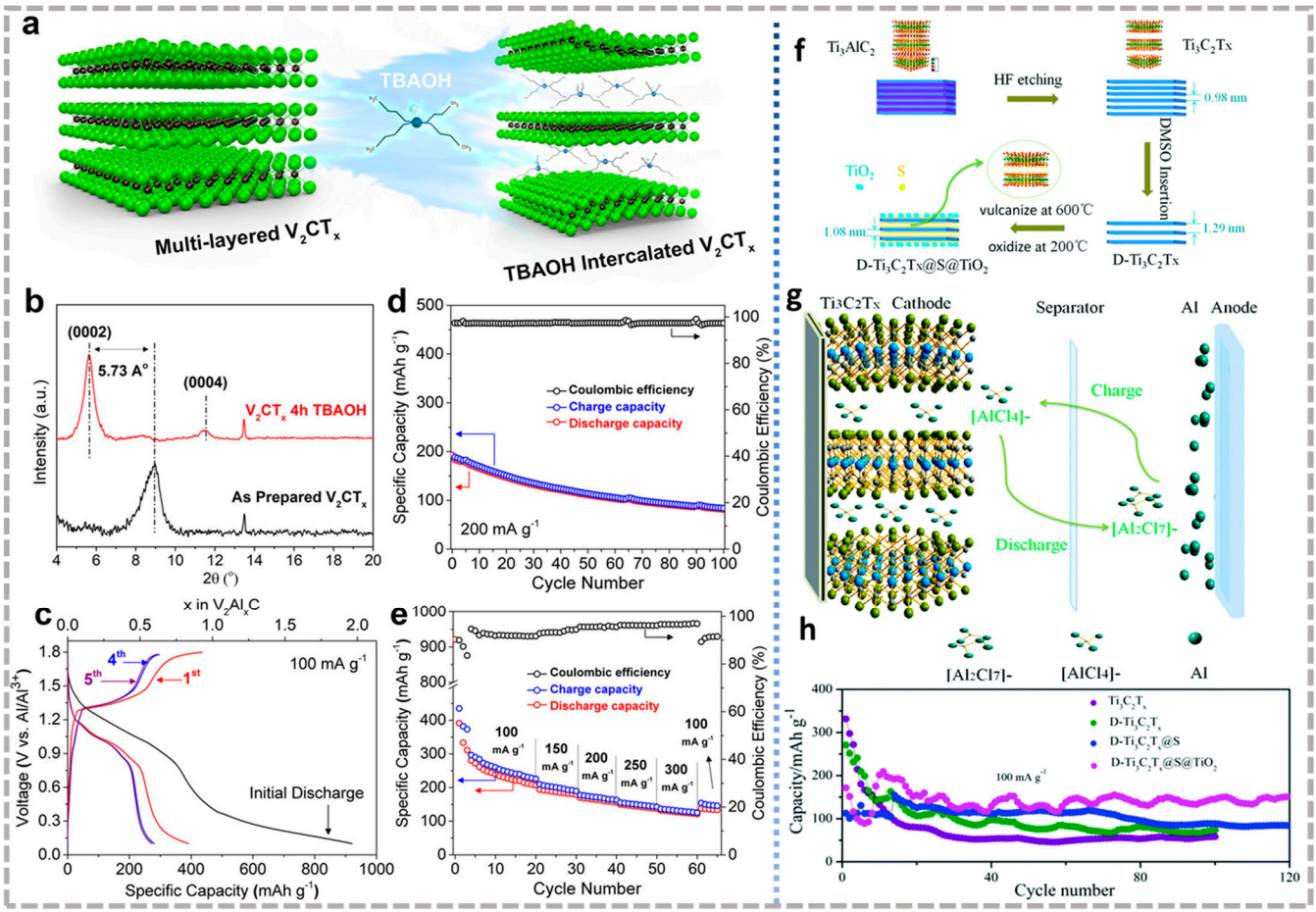

Figure 8. (**a**) Schematic diagram of TBAOH intercalated ML-V_2CT_x for interlayer expansion; (**b**) XRD patterns of ML-V_2CT_x and TBAOH treated ML-V_2CT_x, showing an increased interlayer spacing of about 5.73 Å after TBAOH treatment; (**c**) Charge/discharge curves of TBAOH treated ML-V_2CT_x for the first five cycles; (**d**) Cycling performance of TBAOH treated ML-V_2CT_x cathode over 100 cycles at 200 mA g^{-1}; (**e**) Rate performance of a TBAOH treated ML-V_2CT_x cathode [111]. (**a**–**e**) Reproduced with permission from ACS Nano. (**f**) Schematic diagram of the synthesis process of D-$Ti_3C_2T_x$@S@TiO_2; (**g**) The working mechanism of $Ti_3C_2T_x$ as a cathode material for AIBs; (**h**) Cycling performances of D-$Ti_3C_2T_x$@S@TiO_2 [114]. (**f**–**h**) Reproduced with permission from RSC Pub.

3.3. Calcium Ion Batteries (CIBs)

Ca^{2+} carries two units of positive charge like Mg^{2+}, and Ca is the fifth most abundant element in Earth's crust, with low polarization and low reduction potential (−2.87 V), making it a promising energy system [115]. However, CIBs have developed slowly since their discovery. In the 1990s, Aurbach et al. [116] found that the dissolution/deposition of Ca^{2+} on calcium/precious metal electrodes is impossible due to the fact that the formed surface film has no Ca^{2+} transport properties. In 2016, Ponrouch et al. [117] achieved reversible dissolution/deposition of Ca^{2+} in $Ca(TFSI)_2$, $Ca(ClO_4)_2$, or $Ca(BF_4)_2$ electrolytes using EC: PC as a solvent, that CIBs research showed signs of recovery. Therefore, the

research of CIBs is in an embryonic state, and the report of MXene for CIBs is only in the theoretical research stage as well. Because the electronic shielding layer of Ca^{2+} is not as strong as Mg^{2+}, Ca^{2+} partially forms a second adsorption layer on the basis of forming at least one stable adsorption layer on the surface of MXene [55]. Through theoretical calculations, it is shown that Ti_2CO_2 has a theoretical calcium storage capacity of 487 mAh g^{-1}, which is slightly lower than Mg^{2+} since the increased relative atomic mass, but it can still be comparable to defective graphene materials [55]. Later, Dunda et al. [118] calculated that the V_3C_2/graphene composite structure has a calcium storage capacity of 598.63 mAh g^{-1}. Demiroglu et al. [119] calculated that the theoretical calcium storage capacities of V_2CO_2/graphene and Ti_2CO_2/graphene were 411.31 mAh g^{-1} and 416.39 mAh g^{-1}, respectively, which were significantly higher than their theoretical lithium storage capacity. Further altering the surface terminals, V_2CSe_2 [120] exhibited a maximum theoretical capacity of 394.12 mA h g^{-1} for Ca^{2+} storage.

The applications of MXene in MIBs, AIBs, and CIBs are summarized in Table 3. It can see that although MXenes' ability to store calcium has been theoretically demonstrated, there is still a certain distance from practical application considering the adaptation of electrode materials to electrolytes.

Table 3. Applications of MXene and MXene-based composites in MIBs/HMLBs, AIBs, CIBs.

Material		Cycling Performance			Rate Performance Capacity (mAh g^{-1})	Ref.
		Ion Storage System	Current Density (mA g^{-1})	Initial Capacity (mAh g^{-1})		
MXene	Ti_2CO_2	MIB	/	570	/	[55]
	$Ti_3C_2T_x$/CTAB	MIB	50	100	42 at 1 A g^{-1}	[40]
	$Mg_{0.21}Ti_3C_2T_x$	MIB	50	210	55 at 0.5 A g^{-1}	[86]
	$Ti_3C_2T_x$@C	MIB	10	198.7	123.3 at 0.2A g^{-1}	[88]
	$Ti_3C_2T_x$/CNT	HMLB	10	105	~50 at 1 A g^{-1}	[102]
	Prelithiated-V_2C	HMLB	20	230.3	260.7 at 1 A g^{-1}	[103]
	Ti_3C_2/CTAB	HMLB	100	119.5	100.5 at 2 A g^{-1}	[104]
	Ti_2CO_2	AIB	/	552	/	[55]
	V_2CT_x	AIB	100	162	~150 at 0.3 A g^{-1}	[111]
	Fe_2CS_2	AIB	/	642	/	[112]
	Ti_2CO_2	CIB	/	487	/	[55]
	V_3C_2/graphene	CIB	/	598.63	/	[118]
	V_2CO_2/graphene	CIB	/	411.31	/	[119]
	Ti_2CO_2/graphene	CIB	/	416.39	/	[119]
	V_2CSe_2	CIB	/	394.12	/	[120]
MXene-based composites	$MoS_2/Ti_3C_2T_x$	MIB	50	165	93 at 0.2A g^{-1}	[89]
	TiS_2/Ti_3C_2	MIB	50	97	/	[90]
	$Ti_3C_2/CoSe_2$	MIB	20	114.5	75.7 at 1A g^{-1}	[91]
	VS_4@Ti_3C_2/C	MIB	50	492	129 at 1A g^{-1}	[92]
	LTO NSs@d-Ti_3C_2	MIB	20	320	42 at 0.3A g^{-1}	[93]
	MnO_2/V_2C	MIB	100	130	25 at 0.5A g^{-1}	[94]
	Ti_3C_2@CTAB-Se	AIB	100	583.7	68.1 at 0.3A g^{-1}	[113]
	D-$Ti_3C_2T_x$@S@TiO_2	AIB	100	209.2	51.8 at 0.5A g^{-1}	[114]
Classic cathode material	MoS_2	MIB	50	62	/	[89]
	TiS_2	MIB	50	58	/	[90]

3.4. Zinc-Ion Batteries (ZIBs)

3.4.1. Anode

Compared to other polyvalent ions, the high redox potential (−0.76 V) of Zn makes it possible to use water as an electrolyte solvent, greatly enhancing the safety of the battery [121]. As the hydrophilicity of MXene can promote the penetration of aqueous electrolytes, the application of MXene in aqueous ZIBs far exceeds other MMIBs. However, the commonly used zinc anode is prone to generate dendrites similar to Li during the dissolution/deposition in aqueous electrolytes and suffered from side reactions such as corrosion and hydrogen evolution, which seriously affects the safety and lifespan of the ZIBs [122]. The essence of dendrite formation lies in the uneven zinc nucleation site, and the "top effect" aggravates this phenomenon into a vicious circle [123]. At present, surface modification, structural design, alloyed anode, intercalated anode, and electrolyte modification methods have been used to improve the surface uniformity of zinc anode [122]. As a category of two-dimensional layered materials with excellent conductivity, hydrophilicity, and extensive specific surface area, MXene has the hope of promoting uniform zinc deposition in all these aspects.

The structural design of zinc anode is one of the effective methods to reduce dendrite growth. In aqueous ZIBs, the purpose of structural optimization is to alleviate the formation of zinc dendrites by reducing the local current density and further achieving the homogenization of the surface electric field [124]. The most common method is to load Zn onto a highly conductive substrate by electrodeposition to form a composite material. MXene's high conductivity is considered a good conductive substrate. Tian et al. [125] prepared a $Ti_3C_2T_x$@Zn paper electrode by electrochemically depositing Zn onto $Ti_3C_2T_x$, which replaced Zn as the anode of ZIBs, showing a much better cycling performance. Good electrolyte infiltration of $Ti_3C_2T_x$@Zn guaranteed by $Ti_3C_2T_x$ and fast electron transport channels and ion diffusion channels provided by the layered composite structures endow $Ti_3C_2T_x$@Zn with uniform charge distributions (Figure 9a,j). When 1 mAh cm^{-2} is deposited at 1 mA cm^{-2}, the surface remains smooth and dendritic free (Figure 9b–i). On this basis, shifting the 2D structure to 3D can further promote the uniform Zn^{2+} concentration on the Zn surface by shortening the ion migration pathway. Chen et al. [126] first prepared a 3D porous structure (MGA) by freeze-drying MXene ($Ti_3C_2T_x$) and graphene aerogel and then used it as an electrodeposition matrix to prepare MGA@Zn anodes. Thanks to the formation of ZnF_2-rich solid electrolyte interface (SEI) induced by the -F terminal and inhibited side reactions by composite structure, MGA@Zn has a flat zinc deposition layer even at 10 mA cm^{-2}. Zinc powder with a large specific surface area and abundant electroactive sites has been widely used as the anode of ZIBs [127]. However, the increase of the surface area aggravates the thermodynamic and kinetic instability of zinc in the weak acidic electrolytes, which will produce a violent hydrogen evolution and corrosion reaction, so zinc powder is usually mixed with other materials to make a zinc powder composite anode. Zhi et al. [128] obtained the $Ti_3C_2T_x$@Zn electrode by $Ti_3C_2T_x$ wrapping zinc powder through a solution mixing method.

Zinc surface modification is another strategy to improve the performance of zinc anodes. The aim is to achieve uniform zinc nucleation and a flat deposition layer on the surface of the zinc foil by constructing artificial interface layers [129]. Niu et al. [130] coated $Ti_3C_2T_x$ on the surface of zinc foil(MZn) by self-assembly for the first time, inducing a homogeneous zinc deposition process. After this, various modified Mxene as a surface modification layer began to emerge. Zhi et al. [131] proposed a rare halogen-containing terminal Mxene as an artificial interface layer to regulate zinc deposition, and prepared ($Ti_3C_2Cl_2$, $Ti_3C_2Br_2$, and $Ti_3C_2I_2$)@Zn composite anodes. Ti_3C_2@Zn heterogeneous structure, coupled with ion adsorption with orderly regulation of halogen terminals, jointly promote uniform deposition of zinc planes (Figure 9k,l). It is worth noting that good results can only be achieved when the lattice is matched between Mxene and metal anode, such as $Ti_3C_2Cl_2$@Zn is the best performance here. It can cycle stably for 840 h at 2 mA cm^{-2} at a capacity of 1 mAh cm^{-2}, and the polarization voltages are only 103 mV at 10 mA cm^{-2}(Figure 9m,n). The emergence of this study has given researchers more inspiration. The zinc-ion full battery assembled with Zn/Co co-doped MnO/C (ZnCo-MnO/C) as the cathode, and $Ti_3C_2Cl_2$@Zn as the anode attain at least 3000 cycles at 3.0 A g^{-1}, showing good stability [132]. Qian et al. [133] constructed a composite protective film from MXene composite materials. First, S-loaded $Ti_3C_2T_x$ (S@$Ti_3C_2T_x$) is combined with Zn, and then the S-doped $Ti_3C_2T_x$ and ZnS composite film are obtained by high-temperature treatment, which is anchored on the zinc surface (S/$Ti_3C_2T_x$@ZnS@Zn) as a protective layer. S-$Ti_3C_2T_x$ can effectively instruct uniform zinc deposition by uniform surface electric field distribution, reducing local current density, and mitigating volume changes during charge and discharge. The function of ZnS is to accelerate Zn^{2+} migration, further promote the homogenization of Zn^{2+} concentration, and inhibit side reactions (such as passivation, corrosion, H_2 precipitation, etc.). The synergy between them additionally improves the stability of the surface protection film. This anode with a multifunctional composite interface coating is assembled into a symmetrical battery with good rate performance and cycle stability (up to 1600 h at 0.5 mA cm^{-2} under 0.5 mAh cm^{-2}). Feng et al. [134] designed a flexible artificial protection interface based on self-assembled $Ti_3C_2T_x$ nanosheets and chitosan

(MX/CS) through a simple blade casting strategy, which achieved high reversibility of zinc metal anodes.

The zinc-preferred nucleation sites and uniformly interface electric field provided by the alloyed anode [127] make it a practical and effective solution for dendrite-free ZIBs. However, the violent volume expansion of such materials in the process of alloying/dealloying can easily lead to the crushing and collapse of the material structure, resulting in a sharp attenuation of material capacity. Qian et al. [135] obtained the $Ti_3C_2T_x$@Sb-300 composite backbone by annealing the product acquired through the substitution reaction of $SbCl_3$ with $Ti_3C_2T_x$@Zn. The volume expansion during cycling is effectively mitigated by the introduction of flexible $Ti_3C_2T_x$, which additionally increases the overall integrity and conductivity of the material. The original Sb electrode exhibits rapid capacity degradation, with only 136 mA h g^{-1} capacity left after 100 cycles. Conversely, with similar initial capacities, the $Ti_3C_2T_x$@Sb-300 maintained 299.6 mAh g^{-1} even after 200 cycles, indicating a significant improvement in cycle performance.

The Zn^{2+} insertion/extraction potential of intercalation anodes is generally higher than that of zinc deposition/dissolution potential, which can effectively avoid dendrite problems. MXene is often used as a modified material to compound with other intercalation anodes to improve the performance of the original material. $(NH_4)_2V_{10}O_{25}\cdot 8H_2O$@$Ti_3C_2T_x$ (NHVO@$Ti_3C_2T_x$) [136] and $Ti_3C_2T_x$-TiS_2 [137] are practically used in "rocking chair" ZIBs by Yuan's group and Ni's group. $Ti_3C_2T_x$'s conductive structure and stabilizing effect on the material give the composite a competitive rate performance and excellent long-cycle stability.

Zn^{2+} is carried by electrolyte, so the significance of the electrolyte is obvious. Thus, using of electrolyte additives to control the deposition/dissolution behavior of Zn^{2+} is also an irreplaceable strategy. $Ti_3C_2T_x$ [138] was first used as an electrolyte additive to guide uniform Zn deposition by controlling the nucleation and growth process of Zn. $Ti_3C_2T_x$ adsorbed on Zn foils, inducing uniform initial Zn deposition by providing abundant nucleation –O terminals and subsequently participating in the formation of an intact solid electrolyte interface (SEI) film. At the same time, ion transport can be accelerated to reduce the Zn^{2+} concentration gradient at the electrode/electrolyte interface. The symmetrical battery containing $Ti_3C_2T_x$ is stable to 1180 cycles at 2 mA cm^{-2} under 1 mAh cm^{-2} capacity (only 118 cycles without $Ti_3C_2T_x$). Because of the problems in the aqueous solutions mentioned above, alternative non-liquid electrolytes (hydrogels and solid electrolytes, etc.) have been widely experimented with for ZIBs. Due to the low water content of the non-liquid electrolyte, the adverse side reactions (corrosion and passivation) caused by the presence of H_2O molecules were avoided effectively. The key to high-performance non-liquid electrolytes is the conductive property, so high-ionic conductivity additives are often needed. Zhi et al. [139] added $Ti_3C_2T_x$ of surface-grafted polymethyl acrylate ($Ti_3C_2T_x$-g-PMA) to the polyvinylidene fluoride-hexafluoropropylene (PVHF) solid polymer electrolyte (SPE), and the grafting of PMA was to improve the compatibility of PVHF with $Ti_3C_2T_x$. $Ti_3C_2T_x$ greatly improves the ion conduction of SPE while reducing the crystallinity of the polymer. The SPE added by $Ti_3C_2T_x$ can achieve a Zn^{2+} ion conductivity of 2.69×10^{-4} S cm^{-1} at room temperature, and reversible dendrite-free plating/stripping for over 1000 h.

Because of MXene's large specific surface area and high conductivity, it can reduce the local current density as an electrodeposition substrate or electrolyte additive, make the electric field on the surface of Zn more uniform, and achieve dendrite-free zinc deposition. Its abundant surface activity makes it easy to be perfectly compatible with other materials. When it is used as a composite material for surface modification, accommodation of alloyed anodes, and construction of embedded anodes, it can achieve a more uniform Zn^{2+} distribution, giving the battery excellent zinc deposition stability.

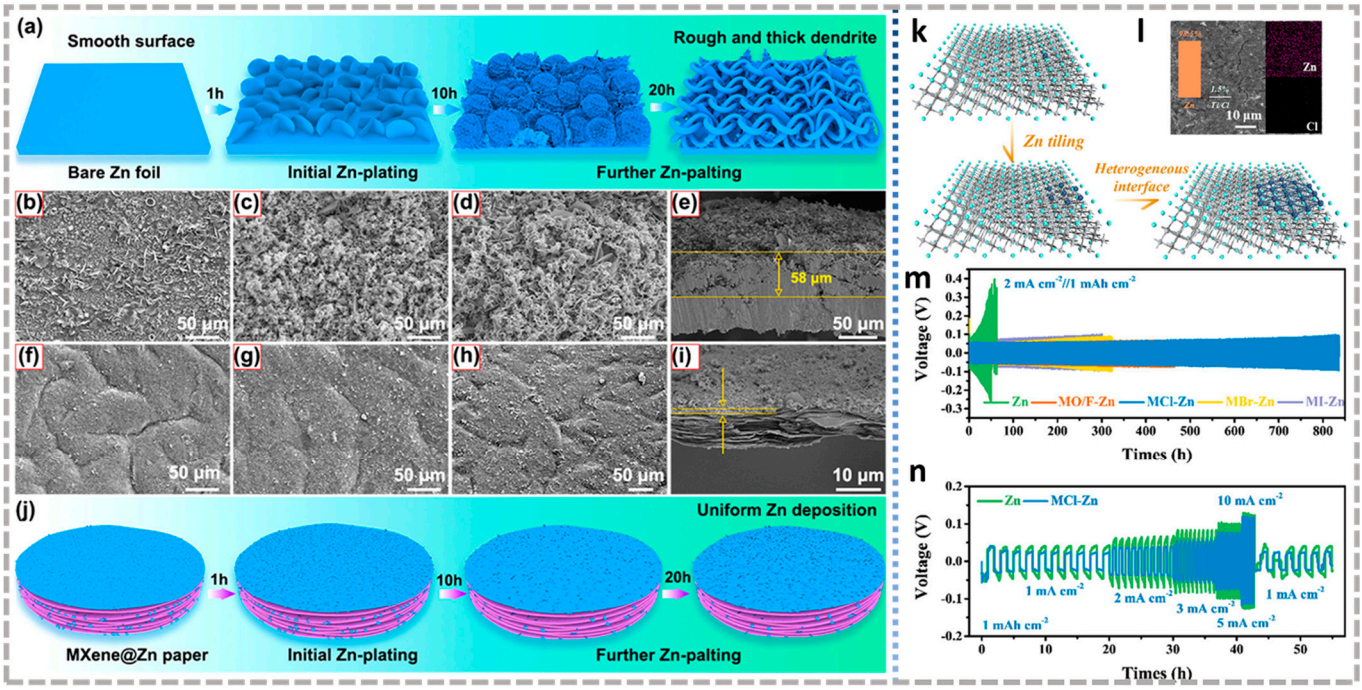

Figure 9. Schematic diagram of Zn deposition on the (**a**) Zn foil and (**j**) $Ti_3C_2T_x$ MXene@Zn paper; SEM images of Zn deposition after plating capacity up to (**b**,**f**) 1, (**c**,**g**) 10, (**d**,**h**) 20 mAh cm^{-2} on Zn foil and Ti_3C_2Tx MXene@Zn paper at 1 mA cm^{-2}, respectively; Cross-sectional SEM images of (**e**) Zn foil and (**i**) $Ti_3C_2T_x$ MXene@Zn paper corresponding to d and h, respectively [125]. (**a**–**j**) Reproduced with permission from ACS Nano. (**k**) Schematic illustration of the Zn deposition process on $Ti_3C_2Cl_2$; (**l**) SEM images and EDX mapping of the $Ti_3C_2Cl_2$-Zn electrode after cycling with a flat and smooth surface; (**m**) Long cycling performance of symmetric batteries; (**n**) Comparison of rate performance of bared Zn metal and $Ti_3C_2Cl_2$–Zn symmetric batteries with a capacity of 1 mAh cm^{-2} [131]. (**k**–**n**) Reproduced with permission from ACS Nano.

3.4.2. Capacitive Electrode

In addition to solving the problem of zinc anodes, the researchers also explored MXene's own zinc storage activity. Zeng's group [140] used MnO_2–CNTs as the cathode and $Ti_3C_2T_x$ as the anode for charge/discharge tests, demonstrating the energy storage characteristics of hybrid capacitors. Furthermore, MXene is widely used in the field of flexible electronics because of its flexibility. Therefore, they further assembled δ-MnO_2 on carbon cloth (δ-MnO_2@CAC) and $Ti_3C_2T_x$ on cotton cloth (MXene@COC) to prepare flexible zinc-ion hybrid capacitors(ZIHCs) [141]. The $Ti_3C_2T_x$, which exhibits the capacitance effect of zinc storage, keeps the power density of hybrid capacitors at a high level, even when used as cathodes in ZIHCs. Wang et al. [142] manufactured Ti_3C_2-Zn hybrid capacitors by combining Ti_3C_2 and Zn. To take the conductivity of MXene to the next level, N-doped Ti_3C_2 (N-Ti_3C_2) [143] was synthesized by a one-step hydrothermal method using urea as a N source. Compared with the C element, the additional electrons of N increase the conductivity of the material and increase the repulsion between layers, which inhibits the self-stacking trend of MXene material and gives the material good stability. The N-Ti_3C_2/Zn hybrid capacitors prepared with N-Ti_3C_2 as the cathode, Zn as the anode, and $ZnSO_4$ as the electrolyte had a discharge capacitance of 247.9 F g^{-1} and an energy density of 45.54 Wh kg^{-1} at 0.1 A g^{-1}. In addition to heteroatom doping, mixing with carbon materials is also a commonly used way to improve conductivity. Wang et al. [144] prepared $Ti_3C_2T_x$-reduced graphene oxide ($Ti_3C_2T_x$-rGO) as a cathode in ZIHCs, improving the conductivity of MXene by adding carbon materials. $Ti_3C_2T_x$-rGO shows a high capacitance of 128.6 F g^{-1} at 0.4 A g^{-1}. Song et al. [145] prepared a DV_2C@CNT cathode by adding carbon nanotubes (CNTs), which exhibit a high capacity of 190.2 F g^{-1} at 0.5 A g^{-1} with

excellent rate performance and durability. Maughan et al. [146] prepared pillared Ti_3C_2 by in situ embedding CTAB, which showed higher capacity when assembled with a zinc anode to form a hybrid capacitor. The main reason is that the embedding CTAB increases the layer spacing of Ti_3C_2, which brings more adsorption site exposure. Fan et al. [147] also prepared Ti_3C_2-Zn hybrid capacitors, but he proposed for the first time that 3D printing technology improved the topography of Ti_3C_2, providing optimized carrier transport, simple electrolyte permeation, and sufficient porosity. The application of 3D printing technology in MXene provides the possibility for more MXene shapes. Although these hybrid capacitors have excellent performance, the application of zinc anodes still faces dendrite risks. Therefore, referring to the method mentioned above, Li et al. [148] showed a cycle life of more than 10,000 times at 3.3 A g^{-1} by alkalizing MXene-Zn composite (AMX-Zn) as the anode matched with the porous carbon as the cathode. Zhi et al. [149] used electrodeposited Zn@Ti_3C_2 anodes to improve the zinc anode cycling problem in the Ti_3C_2-Zn system.

3.4.3. Composite Redox Cathode

It can be seen that MXene's storage of Zn^{2+} exhibits capacitive behavior, and the early application of MXene to ZIBs redox cathodes was achieved by constructing composite materials with known ZIBs active materials. In the composite system, the high conductivity of MXene can ensure the rapid transfer of electrons in the electrode and improve the rate characteristics and utilization rate of the active material. The active material is uniformly loaded on the MXene matrix, and the structural stability is effectively improved, which is conducive to improving cycling performance.

Manganese-Based Material/MXene

Most of the cathode materials of ZIBs belong to transition metal oxides, such as redox materials based on manganese (Mn^{4+}/Mn^{2+}) and vanadium (such as V^{5+}/V^{4+} in V_2O_5). Manganese oxides always suffer severe structural transformations, which will lead to large volume expansions and structural collapse during cycling. MXene can stabilize the structure by providing a stable support framework. Yan et al. [100] prepared 3D $Ti_3C_2T_x$@MnO_2 composites by vapor spray drying a mixed solution of $Ti_3C_2T_x$ and manganese nitrate. $Ti_3C_2T_x$ protects MnO_2 inside and forms a surface fold spherical shape under the impact of spray hot air flow, effectively constructing a solid and conductive 3D microflower structure (Figure 10a–c). The 3D structure improves the wettability of the electrolyte, and the high conductivity of $Ti_3C_2T_x$ builds a three-dimensional conductive network, which greatly improves the dynamic properties of the material (Figure 10d,e). At the same time, the special 3D structure avoids the self-stacking of $Ti_3C_2T_x$ in the cycle, and the material stability is improved. When used as ZIBs cathode, $Ti_3C_2T_x$@MnO_2 microflowers demonstrate a high reversible capacity (~301.2 mA h g^{-1} at 100 mA g^{-1}), excellent rate capability and excellent cycle stability over 2000 cycles (Figure 10f,g). Luo et al. [150] obtained MnO_x@$Ti_3C_2T_x$ composite materials by uniformly growing manganese oxide (MnO_x) on $Ti_3C_2T_x$ two-dimensional surface by hydrothermal method. The MnO_x@$Ti_3C_2T_x$ composite retains $Ti_3C_2T_x$'s layered structure, similar to a parallel circuit. This parallel circuit distributes the current evenly in the layers to increase the upper limit of the electrode's current tolerance, resulting in excellent zinc storage at high current densities. When the current density increases from 0.1 A g^{-1} to 10 A g^{-1}, the capacity retention rate of the MnO_x@$Ti_3C_2T_x$ cathode is 50%. However, the specific capacity is only 82.5 mAh g^{-1} at 0.1 A g^{-1}. In addition to manganese oxides, $ZnMn_2O_4$(ZMO), a zinc-rich cathode that realizes charge storage by reversible with MnO_2, has been widely studied. However, during the cycle of ZMO, it is plagued by structural degradation (agglomeration and dissolution) and side reactions (ZnO generation), resulting in serious capacity loss during long cycles. Peng et al. [151] successfully synthesized ZMO@$Ti_3C_2T_x$ composite structures by freeze-drying them after using the hydrothermal method. $Ti_3C_2T_x$ inhibits the structural degradation and side reactions of ZMO while improving its kinetic performance and realizing long-cycle performance (92.4% capacity retention after 5000 cycles). In addition to

compounding with Ti-based MXene, Zhu et al. [152] also uniformly anchored MnO_2 to K-embedded V_2CT_x (K-V_2C) by hydrothermal method. The K-V_2C@MnO_2 material remains 119.2 mAh g^{-1} capacity in long-term cycles (10,000 cycles) even at 10 A g^{-1}.

Vanadium-Based Materials/MXene

Similar to manganese oxide materials, vanadium oxide materials have poor intrinsic conductivity and vanadium dissolution problems, resulting in suboptimal cycle life and rate performance. As the first discovered MXene material, $Ti_3C_2T_x$ was first used to study the composite with V-based zinc storage active materials. Pan et al. [153] prepared $V_2O_5 \cdot nH_2O/Ti_3C_2T_x$ (VOM) 3D flower-like composites by one-step hydrothermal method and freeze-drying. H_2O embedding V_2O_5 and 3D structures provide rich active sites, laying the foundation for the realization of high capacity [154]. The excellent kinetic properties provided by $Ti_3C_2T_x$ confer excellent rate properties on the composite cathode material (225 mAh g^{-1} at 2 A g^{-1}). The alleviation of V_2O_5 deformation during cycling by the 3D structure was synergistic with the stabilization of the composite structure, achieving 60 mAh g^{-1} capacity, which remained after 500 cycles at 1 A g^{-1}. At the same time, they also paid attention to the ratio of composites, and the lowest charge transfer impedance can be achieved with sufficient active sites at 20 wt% $Ti_3C_2T_x$. In addition, the high average valence state (4.67) of mixed V^{5+}/V^{4+} in $H_2V_3O_8$ can accommodate many inserted Zn^{2+}. Wu et al. [155] constructed $H_2V_3O_8$/MXene composites by one-step hydrothermal method and freeze-drying. The composite structure provides a large number of feasible paths for the diffusion of Zn^{2+} and H_2O, and in synergy with the high conductivity of MXene, the composite exhibits 365 mAh g^{-1} at 0.2 A g^{-1} (306 mAh g^{-1} for $H_2V_3O_8$), higher rate performance of 73 mAh g^{-1} at 20 A g^{-1} (24 mAh g^{-1} for $H_2V_3O_8$), and better cycling performance up to 5600 cycles at 5 A g^{-1} (only 900 cycles for $H_2V_3O_8$). However, Wei et al. [156] synthesized a flexible, independent $VO_2/Ti_3C_2T_x$ hybrid film with a three-dimensional interleaved network using only ultrasound methods. Unlike constructing the 3D structure, Guo et al. [157] designed the $Ti_3C_2T_x$ MXene layer on the surface of the V_2O_5 nanoplate (VPMX) by van der Waals self-assembly method under ultrasound to inhibit vanadium dissolution in the electrochemical process, thereby greatly improving its zinc-ion storage performance.

With the deepening of MXene research, the research of V-matrix active materials and V-based MXene composites began to appear. Interestingly, because it contains the same metallic elements, V-based MXene can be used not only as a frame structure but also as a precursor material. MXene's easy oxidation allows it to partially or completely oxidize to form vanadium oxide active materials. The first to exploit the instability of MXene materials in ZIBs was Zhi et al. [158], who found a large capacity increase during cycling when they used V_2CT_x as the cathode of aqueous zinc/lithium-ion hybrid batteries. The co-embedding of Li^+/Zn^{2+} increases the layer spacing, which in turn peels off V_2CT_x, exposing more active sites and exposing V to the electrolyte. During the cycling process, V_2CT_x is partially oxidized to V_2O_5, which is equivalent to in situ conversion to generate V_2O_5/V_2CT_x, greatly improving the capacity and rate performance of the material (Figure 10h,i). This discovery has inspired researchers, and a large number of research protocols have emerged to activate the zinc storage performance of V-based MXene in recent years. Chou et al. [159] achieved the transition from V^{2+}/V^{3+} to V^{4+}/V^{5+} on the surface of V_2CT_x by precisely controlling the voltage (1.8V) and activation time (2h), which is a process of electrochemical in situ oxidation to form a VO_x/V_2CT_x composite structure. The activated VO_x/V_2CT_x cathode showed a high capacity (423.5 mAh g^{-1} at 1 A g^{-1}) and excellent rate performance (358 mAh g^{-1} at 30 A g^{-1}). Later, Narayanasamy et al. [160] generated V_2O_5@V_2C by partially oxidizing V_2CT_x through controlling hydrothermal conditions (180 °C, 12 h), achieving high-performance Zn^{2+} storage. Tian et al. [161] used V_2CT_x as a precursor to oxidize V_2CT_x by one-step annealing to prepare a porous two-dimensional V_2O_5 material. V_2O_5 inherits the V_2CT_x accordion-like structure and has good structural stability, which guarantees fast charge transport and reversible transport of zinc ions. In addition, Qin et al. [162] achieved the oxidation of V_2CT_x using a high temperature during in situ

generation of HF. The V_2O_x@V_2CT_x was directly synthesized by etching V_2AlC at 90 °C by NaF+HCl.

Chen et al. [95] successfully synthesized VO_2@V_2CO_x by combining hydrothermal and electrochemical oxidation. They first prepared VO_2@V_2C heterostructures by hydrothermal reactions of V_2C with H_2O_2 mixtures. Compared with traditional methods, the shorter length of the prepared VO_2 nanorods shortens the diffusion path. Coupled with the good conductivity and wettability of the V_2C frame, the VO_2@V_2C rate performance and stability are improved, but the performance in terms of capacity is not satisfactory. Therefore, they prepared a VO_2@V_2CO_x by increasing the electrode working voltage activation V_2C with reference to the electrochemical activation method, and the capacity was greatly improved while maintaining the rate of performance (327 mAh g^{-1} at 5 A g^{-1}).

When the V_2CT_x is oxidized, the ion intercalation can also be performed synchronously, so as to combine the advantages of the two modification methods to obtain a high zinc storage active cathode material. Shen et al. [163] soaked V_2CT_x powder in NaOH solution to perform Na^+ intercalation of V_2CT_x MXene to increase the layer spacing. Afterwards, the V_2CT_x of the Na^+ intercalation was hydrothermally treated in $ZnCl_2$ and H_2O_2 solution, and Zn^{2+} intercalation and the oxidation of V_2CT_x were realized simultaneously. The generated $Zn_xV_2O_5$ (ZVO) nanoribbons are uniformly distributed on the surface of V_2CT_x, and $Zn_xV_2O_5{\cdot}nH_2O$-V_2CT_x (VC-ZVO) hybrid materials are obtained with high conductivity and large lattice channels. Electrochemical kinetic tests show that the pre-embedded Zn^{2+} effectively increases the lattice spacing of vanadium oxides, while the V^{4+} generated by in situ oxidation can provide more d-electrons, thereby reducing the activation energy of charge transfer at the electrode/electrolyte interface. In addition, the charge redistribution at the heterogeneous interface between ZVO and V_2CT_x weakens the electrostatic interaction of Zn^{2+}, which promotes its diffusion. Therefore, the VC-ZVO electrode shows amazing electrochemical performance, and 96.4% capacity retention can be achieved after 8000 cycles at 10 A g^{-1}. Using a similar method, the same group synthesized pre-embedded composites $Mn_xV_{10}O_{24}{\cdot}nH_2O$@$V_2CT_x$ (MVO@VC), $Li_xV_2O_5{\cdot}H_2O$@V_2CT_x (LVO@VC) and $Al_xV_2O_5{\cdot}$ H_2O@V_2CT_x [164]. As cathode materials for ZIBs, they exhibit improved performance.

In the process of studying the electrochemical in situ oxidation of V_2CT_x, Zhi et al. also found that the XRD peak strength of the residual precursor V_2AlC weakened and disappeared during the cycling process. Therefore, they replaced the cathode material with V_2AlC in the same electrolyte system (21 M LiTFSI + 1 M Zn $(OTf)_2$) [165], with zinc metal as anode assembled into ZIB [166]. During the cycle, V_2AlC is in situ etched into V_2CT_x MXene by a fluorine-rich electrolyte inside the battery. This method is a one-step green etching, peeling method without any acid/alkali to prepare MXene. ZIB always works normally during the etching process and exhibits a gradually increasing specific capacity with the formation of MXene and the oxidation product V_2O_5.

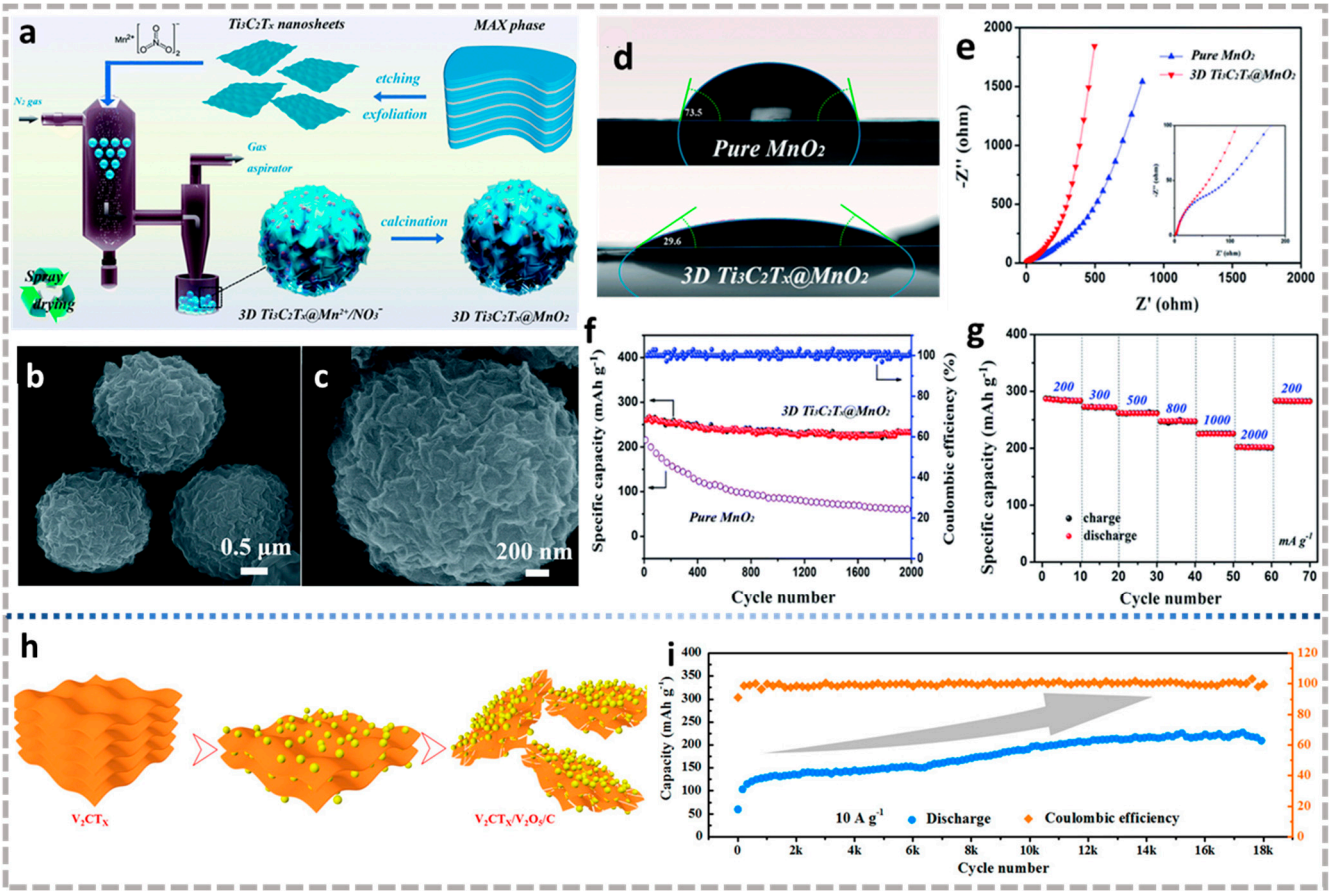

Figure 10. (**a**) Schematic of 3D $Ti_3C_2T_x$@MnO_2 microflower synthesis progress. (**b**,**c**) SEM images of 3D $Ti_3C_2T_x$@MnO_2 microflowers with different magnifications. (**d**) Contact angles of droplets of electrolyte on the surface of MnO_2 and 3D $Ti_3C_2T_x$@MnO_2 microflower. (**e**) Comparison of EIS for MnO_2 and 3D $Ti_3C_2T_x$@MnO_2 microflower cathodes in aqueous ZIBs. (**f**) Long-term cycling stability at 500 mA g^{-1}; (**g**) rate performance of 3D $Ti_3C_2T_x$@MnO_2 microflowers in aqueous ZIBs [100]. (**a**–**g**) Reproduced with permission from the Royal Society of Chemistry. (**h**) Schematic diagram of possible structural changes in the V_2CT_x cathode during cycling. (**i**) Long-term cycling performance of V_2CT_X cathode at 10 A g^{-1} [158]. (**h**,**i**) Reproduced with permission from ACS Nano.

Other Categories Materials/MXene

In addition to Mn-based and V-based cathode materials, MXene materials can also be compounded with other categories of ZIBs cathode materials. Layered transition metal chalcogenides (TMCs) are also potential candidates for ZIBs cathode materials, and low conductivity and collapse-prone layered structures are the main factors plaguing the cycling performance of TMCs. Long et al. [167] synthesized 1 T-MoS_2/Ti_3C_2 heterojunctions by in situ hydrothermal method (Figure 11a), and used them as ZIBs cathode material to demonstrate high capacity, rate performance (284.3 mAh g^{-1} at 0.10 A g^{-1} and 105.2 mAh g^{-1} at 10.00 A g^{-1}) and cycle stability (93.2% capacity retention after 3000 cycles, Figure 11b), all higher than pristine 1 T-MoS_2. The elevated capacity is due to the richer ion storage space caused by the expansion layers of 1 T-MoS_2. Excellent rate capability thanks to ultrafast electron and ion transport from Ti_3C_2. The outstanding long-term cycle stability is attributed to the synergy effect of 1 T-MoS_2 and Ti_3C_2 in 3D interconnected networks. Gao et al. [168] also applied MXene to the MoO_3 cathode with high capacity and low conductivity to prepare MoO_{3-x}/$Ti_3C_2T_x$ composites. MoO_{3-x}/$Ti_3C_2T_x$, as the ZIBs cathode, provides an ultra-large capacity of 369.8 mAh g^{-1} at 0.20 A g^{-1}, maintaining 46.7% capacity after 1600 cycles. Inspired by in situ oxidation of V-based MXene to produce vanadium oxides, Sun et al. [97] proposed a gentle one-step surface selenization strategy,

which has successfully synthesized $VSe_2@V_2CT_x$, $TiSe_2@Ti_3C_2T_x$, and $NbSe_2@Nb_2CT_x$. MXene's surface metal atoms are converted into high-capacity transition metal selenides ($TMSe_2$), while MXene's inner layer is deliberately preserved to improve overall conductivity and structural stability. Typically, $VSe_2@V_2CT_x$ cathode provides a high-rate capability (132.7 mA h g^{-1} at 2.0 A g^{-1}) and long-term cycling capability (93.1% capacity retention at 2.0 A g^{-1} after 200 cycles). Similarly, many cathode materials suffer from low conductivity, including two-dimensional layered double hydroxides (LDHs). Han et al. [169] obtained Co-doped NiMn-LDH@V_2CT_x (CNMV) by a one-step hydrothermal method. V_2CT_x as a frame structure improves the overall conductivity, and the specific capacity of CNMV as ZIBs cathode material is 322.7 mAh g^{-1} after 100 cycles at 0.2 A g^{-1}. In addition to compounding with highly conductive materials, finding active materials with high intrinsic conductivity is also an option. Studies have found that many conductive polymers exhibit energy storage activity. Polyaniline (PANI) has been applied to ZIBs as a typical conductive polymer, but volumetric strain and protonation hinder its stable cycling. Huang et al. [170] used sulfonated group grafting $Ti_3C_2T_x$ MXene (S-$Ti_3C_2T_x$) with high conductivity, good flexibility to composite with PANI. S-$Ti_3C_2T_x$ continuously contributes to protons and locally delivers high acidity, keeping the polymer at a low pH, effectively inhibiting the deprotonation of PANI (Figure 11c). Consequently, high discharge capacity (262 mAh g^{-1} at 0.5 A g^{-1}), excellent rate performance (160 mAh g^{-1} at 15 A g^{-1}, Figure 11d) and cycle stability (more than 5000 cycles) are simultaneously demonstrated on the S-$Ti_3C_2T_x$-enhanced PANI cathode.

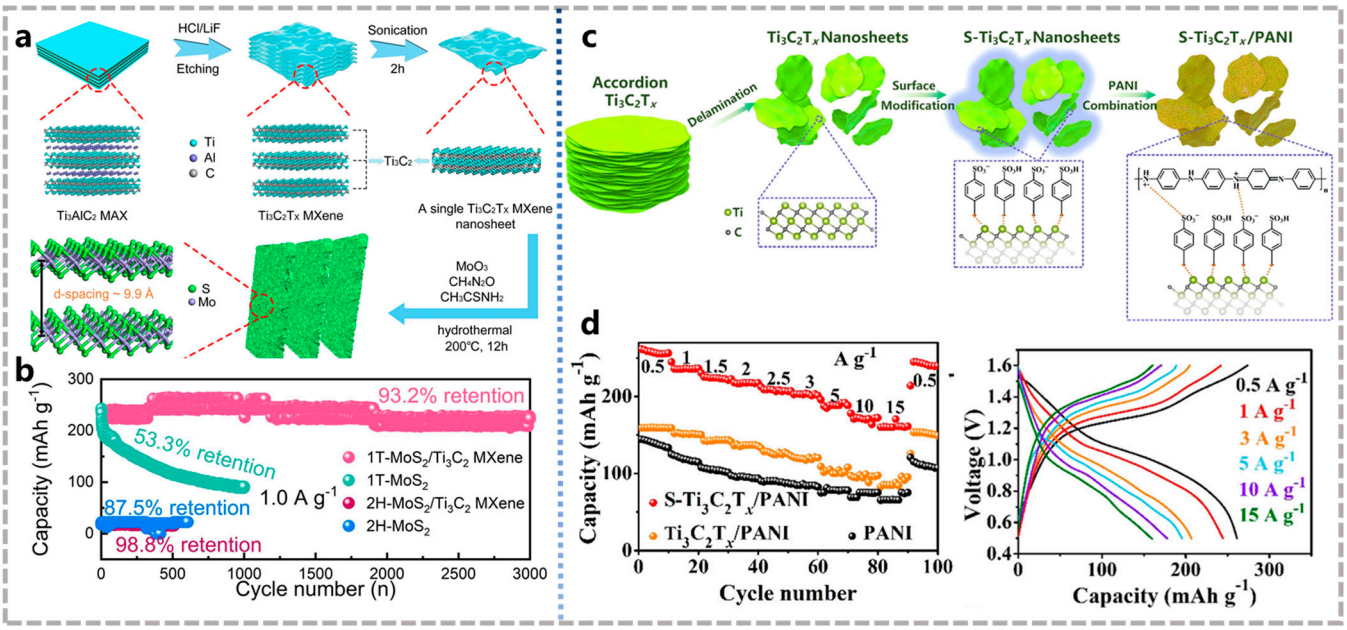

Figure 11. (**a**) Synthesis schematic of 1 T-MoS_2/Ti_3C_2 MXene. (**b**) Cycle performance at 1.00 A g^{-1} of 1 T-MoS_2/Ti_3C_2 MXene and 1 T-MoS_2 [167]. (**a**,**b**) Reproduced with permission from ELSEVIER BV. (**c**) Schematic of S-$Ti_3C_2T_x$/PANI preparation. (**d**) Rate performance of S-$Ti_3C_2T_x$/PANI [170]. (**c**,**d**) Reproduced with permission from ACS Nano.

3.4.4. Redox Cathode

Previous studies have shown that MXene itself exhibits capacitive behavior for Zn^{2+} storage. However, inspired by the conversion of V-based MXene, changes in voltage and surface terminal groups may stimulate the redox behavior of MXene. Nb_2CT_x/Zn battery exhibits capacitive behavior when the voltage is lower than 2.0 V, and Zhi et al. successfully activated the Nb_2CT_x zinc storage voltage platform at 1.55 V by extending the voltage window from 2.0 V to 2.4 V [171]. The results of molecular dynamics simulation tell us that sufficient energy can be assimilated to pierce the embedding barrier when the voltage reaches a certain value. Zn^{2+} is further embedded between layers from simple

surface adsorption to exhibit a redox plateau. They also increased the voltage to activate the redox zinc storage behavior of $Ti_3C_2T_x$, which is expected to be applied to more MXene materials. Because the activation voltage is much higher than the electrochemical window of water (1.23 V), the implementation of this method requires the guarantee of high salt concentration.

The above research on multivalent ion batteries basically focuses on M materials in MXene, and little is known about X materials, let alone T_x, which makes the rich surface chemistry of MXene not reflected in multivalent ion batteries. In 2021, Zhi et al. [172] first studied the effect of terminal groups on the zinc storage performance of Ti_3C_2, and successfully activated the redox activity of Ti_3C_2 by changing the terminal group. As mentioned above, $Ti_3C_2Cl_2$ and Ti_3C_2(OF) exhibit zinc storage capacitance behavior without an obvious plateau. Varying their terminal groups, $Ti_3C_2Br_2$ and $Ti_3C_2I_2$ successfully exhibited different discharge plates with capacities of 97.6 and 135 mAh g^{-1}, respectively (Figure 12). Taking $Ti_3C_2Br_2$ as an example to illustrate its zinc storage mechanism, there is a 2 Br^- −2 $e^- \leftrightarrow$ 2 Br^0 redox reaction during the electrode charge/discharge process, followed by the following reaction $Br^- + (n-1)\,Br^0 \leftrightarrow Br^{n-}$ ($3 \leq n \leq 5$), and finally Zn^{2+} achieves deintercalation/intercalation. The success of this experiment provides strong proof of the surface chemistry of MXene and will greatly increase the confidence of researchers in the exploration of MXene surface chemistry. The applications of MXene in ZIBs are summarized in Table 4.

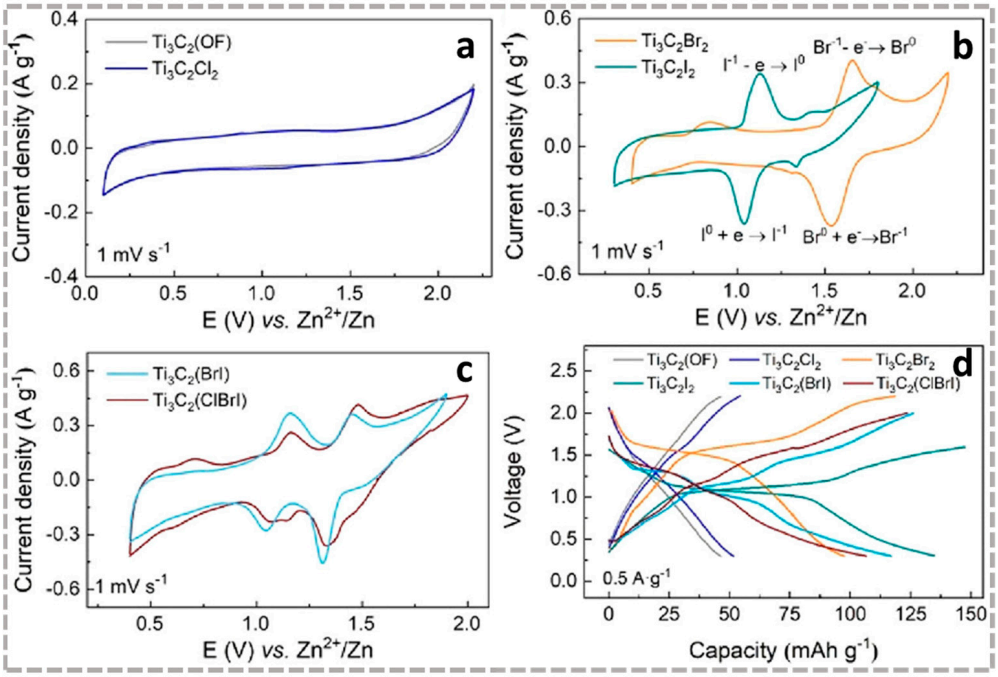

Figure 12. Cyclic voltammetry curve (CV) of (**a**) Ti_3C_2(OF), $Ti_3C_2Cl_2$, (**b**) $Ti_3C_2Br_2$, $Ti_3C_2I_2$, (**c**) Ti_3C_2(BrI), and Ti_3C_2(ClBrI) at 1 mV s^{-1}. (**d**) GCD curves of $Ti_3C_2T_x$ with terminals corresponding to (**a**–**c**) at 0.5 A g^{-1} [172]. (**a**–**d**) Reproduced with permission from ACS Nano.

Table 4. Applications of MXene and MXene-based composites in ZIBs.

Application	Material	Cycling Performance			Rate Performance Capacity (mAh g^{-1}) [Overpotential of Zn Deposition (mV)]	Ref.
		Current Density (A g^{-1})	Capacity Retention (mAh g^{-1})	CycleNumber		
Anode *	$Ti_3C_2T_x$@Zn	1	1	300h	~83 at 1 mA cm^{-2}	[125]
	MGA@Zn	10	1	1050h	~64 at 10 mA cm^{-2}	[126]
	$Ti_3C_2T_x$@Zn	1	0.5	200h	30 at 1 mA cm^{-2}	[128]
	MZn	0.2	0.2	800h	112 at 5 mA cm^{-2}	[130]
	$Ti_3C_2Cl_2$@Zn	2	1	840h	103 at 10 mA cm^{-2}	[131]
	S/$Ti_3C_2T_x$@ZnS@Zn	0.5	0.5	1600h	142 at 10 mA cm^{-2}	[133]
	MX/CS	1	1	2100h	~300 at 10 mA cm^{-2}	[134]
	$Ti_3C_2T_x$@Sb-300	0.5	0.5	1000h	~300 at 10 mA cm^{-2}	[135]
	$Ti_3C_2T_x$ additive	2	1	1180	~160 at 4 mA cm^{-2}	[138]
	$Ti_3C_2T_x$-g-PMA	0.1	0.1	1200h	/	[139]
	NHVO@$Ti_3C_2T_x$	500	331.8	500	135.1 at 5 A g^1	[136]
	$Ti_3C_2T_x$-TiS_2	125.7	129.6	/	97.5 at 1.2566 A g^1	[137]
MXene-based composites	3D $Ti_3C_2T_x$@MnO_2	0.5	237	2000	202.2 at 2 A g^{-1}	[100]
	MnO_x@$Ti_3C_2T_x$	5	50	400	~35 at 10 A g^{-1}	[150]
	ZMO@$Ti_3C_2T_x$	1	159.5	5000	84.5 at 4 A g^{-1}	[151]
	K-V_2C@MnO_2	10	119.2	10,000	87.7 at 15 A g^{-1}	[152]
	$V_2O_5 \cdot nH_2O$/$Ti_3C_2T_x$	0.1	223	50	225 at 2 A g^{-1}	[153]
	$H_2V_3O_8$/MXene	5	159.3	5600	73.1 at 20 A g^{-1}	[155]
	VO_2/$Ti_3C_2T_x$	2	126.6	7000	94.05 at 5 A g^{-1}	[156]
	VPMX	10	~99.5%	5000	243.6 at 5 A g^{-1}	[157]
	V_2CT_x	10	202	16,000	141.8 at 20 A g^{-1}	[158]
	VO_x/V_2CT_x	30	283.7	2000	358 at 30 A g^{-1}	[159]
	V_2O_5@V_2C	4	252.3	2000	290 at 4 A g^{-1}	[160]
	Derivative V_2O_5	2	279	3500	250.4 at 8 A g^{-1}	[161]
	V_2O_x@V_2CT_x	1	87.74	200	84 at 2 A g^{-1}	[162]
	VO_2@V_2CO_x	5	327	1500	327 at 5 A g^{-1}	[95]
	VC-ZVO	10	223.9	8000	184.3 at 20 A g^{-1}	[163]
	MVO@VC	10	287.6	25,000	235.5 at 22 A g^{-1}	[164]
	V_2AlC	5	240	1500	97.5 at 64 A g^{-1}	[166]
	1 T-MoS_2/Ti_3C_2	1	177	3000	105.2 at 10 A g^{-1}	[167]
	MoO_{3-x}/$Ti_3C_2T_x$	4	51.65	1600	110.6 at 4 A g^{-1}	[168]
	VSe_2@V_2CT_x	2	158.1	600	132.7 at 2 A g^{-1}	[97]
	CNMV	0.2	322.7	100	51.4 at 5 A g^{-1}	[169]
	S-$Ti_3C_2T_x$/PANI	15	103	5000	160 at 15 A g^{-1}	[170]
Redox cathode	Nb_2CT_x	1	121	1800	77 at 6 A g^{-1}	[171]
	$Ti_3C_2Br_2$	4	80%	1000	67.2 at 15 A g^{-1}	[172]
	$Ti_3C_2I_2$	4	80%	700	101 at 15 A g^{-1}	[172]
Classic cathode material	MnO_2	0.5	~75	2000	125.4 at 2 A g^{-1}	[100]
	$V_2O_5 \cdot nH_2O$	0.1	142	50	2 at 2 A g^{-1}	[153]
	1 T-MoS_2	1	~100	1000	78.5 at 10 A g^{-1}	[167]

* When used as an anode, the current density unit is mA cm^{-2}, and the capacity unit is mAh cm^{-2}.

In summary, MXene is used independently as an electrode material for MMIBs with the following challenges: slope curves that only reflect capacitive effects, such as the zinc storage process of Ti_3C_2; the low diffusivity brought by the large radius of polyvalent ions, which is most obvious in MIBs; and the problem of the collapse of the structure during cycling caused by the high charge of carriers, which is most obvious in AIBs. Nevertheless, the application of MXene in MMIBs is developing rapidly. The researchers not only explored the multivalent ion storage activity of MXene itself but also utilized the high conductivity and surface activity of MXene as a substrate material and artificial interface layer to achieve excellent cycling and rate performance. Although many excellent results have been achieved, they are generally concentrated in several classes of MXene materials, such as Ti-based (Ti_3C_2, Ti_2C) and V-based (V_2C). The calcium storage activity of MXene is only at the theoretical level, and there is no experimental study to prove it. Research on the surface chemistry of MXene by changing terminals is also limited, as is topography.

4. Conclusions

Herein, we first introduce the synthesis methods of MXene materials, including fluorine-containing and fluorine-free etching methods as well as non-etching methods. Generally, the subsequent peeling process is closely followed, and the obtained few-layer MXene not only avoids agglomeration but also provides more active sites. The stability,

mechanical and electronic properties of MXene were then analyzed. In order to make the MXene material stable, its surface-active sites should be protected as much as possible, and secondly, interlayer stacking can be avoided by expanding layer spacing, constructing three-dimensional structures, and compounding with other materials. The excellent elastic coefficient is a strong contender for flexible electrodes, and the desired electronic properties can also be achieved through the design of terminal groups. Finally, we focus on practical applications in MMIBs. Because of its large specific surface area, hydrophilicity, and high conductivity, it is used as an electrode coating and electrolyte additive, greatly enriching the diversity of MXene applications. We found that MXene has polyvalent ion storage activity, but has the characteristics of low capacity and poor cycling performance. One feasible approach is to activate MXene energy storage activity by electrochemistry or surface terminal groups, and another method is to use intercalated substances or to construct composite materials with other active materials to achieve high capacity, exceptional rate performance, and long-cycle life.

5. Outlooks

The research on MXene materials is rich and diverse, but there is still a long way to go to meet the requirements of industrial production. There are still a number of issues that deserve our attention and need to be addressed urgently.

(1) The stability of MXene material. MXene materials are very sensitive to oxygen and water. The high surface activity makes the layered structure of MXene prone to collapse, and it is important to stabilize MXene materials in practical applications.

(2) Synthesis of MXene material. So far, more than 30 kinds of MXene materials have been discovered, but there are more than 70 MAX precursors. Each MXene has its own unique etching parameters, so matching the synthesis conditions for each MXene is essential to broaden the MXene family.

(3) MXene species. The application of MXene is still only in the common Ti_3C_2, V_2C, etc., but different components of MXene may bring unexpected results. For example, nitrogen-doped carbides and nitride MXene exhibit higher electrical conductivity, while there is little research on nitride MXene due to synthesis difficulty. Therefore, putting more types of MXene into practice is a major topic for subsequent research, in which the issue of cost should also be considered.

(4) Terminal group of MXene material. MXene material has rich surface chemistry, which can change the terminal group to change its properties, thereby broadening the application scenarios. Although MXene materials of various terminal groups such as NH, S, Cl, Se, Br, Te, etc. can be prepared by post-treatment methods, it is still very rare to apply them to practice. The general lack of attention to the terminal groups on the surface undoubtedly deprives MXene materials of a significant advantage.

(5) Composite structure. Because of its high surface activity and high electrical conductivity, MXene is often used to build composite materials with other materials. However, whether all materials can be combined and whether they can have a favorable effect on the performance after compounding should be summarized in this regard. The optimal composite ratio should also be discussed.

(6) Application in MMIBs. Because of the inherent problem of multivalent ions as carriers, there is still a huge space for exploration in the application of MXene in MMIBs. For example, the application of MXene in CIBs is still in the theoretical research stage, and experiments are urgently needed to prove it. The second adsorption layer of MIBs can exhibit dissolution/deposition behavior, and how to release the capacity of this part is also a question worth considering. The problem of actual carriers in AIBs is also worth studying. Whether the method of activating more redox activity of ZIBs can be extended to other materials or other fields will also be an interesting research topic.

(7) MXene exhibits the characteristics of pseudocapacitance in the storage of MMIBs, and although it has high conductivity, its low capacity cannot meet the needs of high-energy devices. Fortunately, composites partially compensate for these shortcomings, but they are

still a long way from practical applications. Commercial $LiFeO_4$ materials can still maintain 90% capacity after more than 6000 cycles at 1 C, while MXene is rarely achieved even based on composite materials. However, because MMIBs are different from LIBs, this comparison is not convincing. Therefore, determining the application scenarios and evaluation criteria of MMIBs is convenient for more objective evaluations. Another limitation is that the amount of material used in the lab is small and the cost is often rarely considered. In this regard, titanium-based MXene is the most attractive because precursors (i.e., Ti, Al, C) are relatively abundant and inexpensive.

To date, there have been many fantastic research works on the application of MXenes in MMIBs. It is believed that the application of MXene will be extended to the fields of supercapacitors and catalysis on the basis of these achievements.

Author Contributions: Conceptualization, X.P. and Z.C.; investigation, C.W. and Z.P.; data curation, C.W. and H.C.; writing—original draft preparation, C.W., Z.P. and H.C.; writing—review and editing, C.W., X.P. and Z.C.; supervision, X.P. and Z.C.; funding acquisition, Z.C. All authors have read and agreed to the published version of the manuscript.

Funding: This work was financially supported by the National Natural Science Foundation of China (21875171 and U22A20438) and the Fundamental Research Funds for the Central Universities.

Institutional Review Board Statement: Not applicable.

Informed Consent Statement: Not applicable.

Conflicts of Interest: The authors declare no conflict of interest.

References

1. Guan, P.; Zhou, L.; Yu, Z.; Sun, Y.; Liu, Y.; Wu, F.; Jiang, Y.; Chu, D. Recent progress of surface coating on cathode materials for high-performance lithium-ion batteries. *J. Energy Chem.* **2020**, *43*, 220–235. [CrossRef]
2. Hussain, I.; Lamiel, C.; Sufyan Javed, M.; Ahmad, M.; Chen, X.; Sahoo, S.; Ma, X.; Bajaber, M.A.; Zahid Ansari, M.; Zhang, K. Earth- and marine-life-resembling nanostructures for electrochemical energy storage. *Chem. Eng. J.* **2023**, *454*, 140313. [CrossRef]
3. Kim, T.-H.; Park, J.-S.; Chang, S.K.; Choi, S.; Ryu, J.H.; Song, H.-K. The Current Move of Lithium Ion Batteries Towards the Next Phase. *Adv. Energy Mater.* **2012**, *2*, 860–872. [CrossRef]
4. Wang, H.; Chen, S.; Fu, C.; Ding, Y.; Liu, G.; Cao, Y.; Chen, Z. Recent Advances in Conversion-Type Electrode Materials for Post Lithium-Ion Batteries. *ACS Mater. Lett.* **2021**, *3*, 956–977. [CrossRef]
5. Ming, F.; Liang, H.; Huang, G.; Bayhan, Z.; Alshareef, H.N. MXenes for Rechargeable Batteries Beyond the Lithium-Ion. *Adv. Mater.* **2021**, *33*, 2004039. [CrossRef]
6. Fang, G.; Zhou, J.; Pan, A.; Liang, S. Recent Advances in Aqueous Zinc-Ion Batteries. *ACS Energy Lett.* **2018**, *3*, 2480–2501. [CrossRef]
7. Kravchyk, K.V.; Widmer, R.; Erni, R.; Dubey, R.J.C.; Krumeich, F.; Kovalenko, M.V.; Bodnarchuk, M.I. Copper sulfide nanoparticles as high-performance cathode materials for Mg-ion batteries. *Sci. Rep.* **2019**, *9*, 7988. [CrossRef]
8. Dymek, C.J.; Williams, J.L.; Groeger, D.J.; Auborn, J.J. An Aluminum Acid-Base Concentration Cell Using Room Temperature Chloroaluminate Ionic Liquids. *J. Electrochem. Soc.* **1984**, *131*, 2887. [CrossRef]
9. Geng, D.; Yang, H.Y. Recent Advances in Growth of Novel 2D Materials: Beyond Graphene and Transition Metal Dichalcogenides. *Adv. Mater.* **2018**, *30*, 1800865. [CrossRef]
10. Li, S.-L.; Tsukagoshi, K.; Orgiu, E.; Samorì, P. Charge transport and mobility engineering in two-dimensional transition metal chalcogenide semiconductors. *Chem. Soc. Rev.* **2016**, *45*, 118–151. [CrossRef]
11. Novoselov, K.S.; Mishchenko, A.; Carvalho, A.; Castro Neto, A.H. 2D materials and van der Waals heterostructures. *Science* **2016**, *353*, aac9439. [CrossRef] [PubMed]
12. Sun, S.J.; Liao, C.; Hafez, A.M.; Zhu, H.L.; Wu, S.P. Two-dimensional MXenes for energy storage. *Chem. Eng. J.* **2018**, *338*, 27–45. [CrossRef]
13. Mateen, A.; Ansari, M.Z.; Hussain, I.; Eldin, S.M.; Albaqami, M.D.; Bahajjaj, A.A.A.; Javed, M.S.; Peng, K.-Q. Ti_2CTx–MXene aerogel based ultra–stable Zn–ion supercapacitor. *Compos. Commun.* **2023**, *38*, 101493. [CrossRef]
14. Naguib, M.; Kurtoglu, M.; Presser, V.; Lu, J.; Niu, J.; Heon, M.; Hultman, L.; Gogotsi, Y.; Barsoum, M.W. Two-Dimensional Nanocrystals Produced by Exfoliation of Ti_3AlC_2. *Adv. Mater.* **2011**, *23*, 4248–4253. [CrossRef]
15. Xu, X.; Zhang, Y.; Sun, H.; Zhou, J.; Yang, F.; Li, H.; Chen, H.; Chen, Y.; Liu, Z.; Qiu, Z.; et al. Progress and Perspective: MXene and MXene-Based Nanomaterials for High-Performance Energy Storage Devices. *Adv. Electron. Mater.* **2021**, *7*, 2000967. [CrossRef]
16. Greaves, M.; Barg, S.; Bissett, M.A. MXene-Based Anodes for Metal-Ion Batteries. *Batter. Supercaps* **2020**, *3*, 214–235. [CrossRef]
17. Cheng, L.; Li, X.; Zhang, H.; Xiang, Q. Two-Dimensional Transition Metal MXene-Based Photocatalysts for Solar Fuel Generation. *J. Phys. Chem. Lett.* **2019**, *10*, 3488–3494. [CrossRef]

18. Naguib, M.; Mashtalir, O.; Carle, J.; Presser, V.; Lu, J.; Hultman, L.; Gogotsi, Y.; Barsoum, M.W. Two-Dimensional Transition Metal Carbides. *ACS Nano* **2012**, *6*, 1322–1331. [CrossRef]
19. Deysher, G.; Shuck, C.E.; Hantanasirisakul, K.; Frey, N.C.; Foucher, A.C.; Maleski, K.; Sarycheva, A.; Shenoy, V.B.; Stach, E.A.; Anasori, B.; et al. Synthesis of Mo_4VAlC_4 MAX Phase and Two-Dimensional Mo_4VC_4 MXene with Five Atomic Layers of Transition Metals. *ACS Nano* **2020**, *14*, 204–217. [CrossRef]
20. Tao, Q.; Dahlqvist, M.; Lu, J.; Kota, S.; Meshkian, R.; Halim, J.; Palisaitis, J.; Hultman, L.; Barsoum, M.W.; Persson, P.O.Å.; et al. Two-dimensional $Mo_{1.33}C$ MXene with divacancy ordering prepared from parent 3D laminate with in-plane chemical ordering. *Nat. Commun.* **2017**, *8*, 14949. [CrossRef]
21. Thörnberg, J.; Halim, J.; Lu, J.; Meshkian, R.; Palisaitis, J.; Hultman, L.; Persson, P.O.Å.; Rosen, J. Synthesis of $(V_{2/3}Sc_{1/3})_2AlC$ i-MAX phase and $V_{2-}xC$ MXene scrolls. *Nanoscale* **2019**, *11*, 14720–14726. [CrossRef]
22. Zhu, J.; Ha, E.; Zhao, G.; Zhou, Y.; Huang, D.; Yue, G.; Hu, L.; Sun, N.; Wang, Y.; Lee, L.Y.S.; et al. Recent advance in MXenes: A promising 2D material for catalysis, sensor and chemical adsorption. *Coord. Chem. Rev.* **2017**, *352*, 306–327. [CrossRef]
23. Naguib, M.; Mochalin, V.N.; Barsoum, M.W.; Gogotsi, Y. 25th Anniversary Article: MXenes: A New Family of Two-Dimensional Materials. *Adv. Mater.* **2014**, *26*, 992–1005. [CrossRef] [PubMed]
24. Anasori, B.; Lukatskaya, M.R.; Gogotsi, Y. 2D metal carbides and nitrides (MXenes) for energy storage. *Nat. Rev. Mater.* **2017**, *2*, 16098. [CrossRef]
25. Yang, S.; Zhang, K.; Ricciardulli, A.G.; Zhang, P.; Liao, Z.; Lohe, M.R.; Zschech, E.; Blom, P.W.M.; Pisula, W.; Müllen, K.; et al. A Delamination Strategy for Thinly Layered Defect-Free High-Mobility Black Phosphorus Flakes. *Angew. Chem. Int. Ed.* **2018**, *57*, 4677–4681. [CrossRef]
26. Naguib, M.; Halim, J.; Lu, J.; Cook, K.M.; Hultman, L.; Gogotsi, Y.; Barsoum, M.W. New Two-Dimensional Niobium and Vanadium Carbides as Promising Materials for Li-Ion Batteries. *J. Am. Chem. Soc.* **2013**, *135*, 15966–15969. [CrossRef]
27. Cui, G.; Zheng, X.; Lv, X.; Jia, Q.; Xie, W.; Gu, G. Synthesis and microwave absorption of Ti_3C_2Tx MXene with diverse reactant concentration, reaction time, and reaction temperature. *Ceram. Int.* **2019**, *45*, 23600–23610. [CrossRef]
28. Liu, F.F.; Zhou, A.G.; Chen, J.F.; Jin, J.; Zhou, W.J.; Wang, L.B.; Hu, Q.K. Preparation of Ti_3C_2 and Ti_2C MXenes by fluoride salts etching and methane adsorptive properties. *Appl. Surf. Sci.* **2017**, *416*, 781–789. [CrossRef]
29. Zhang, T.; Pan, L.M.; Tang, H.; Du, F.; Guo, Y.H.; Qiu, T.; Yang, J. Synthesis of two-dimensional Ti_3C_2Tx MXene using HCl plus LiF etchant: Enhanced exfoliation and delamination. *J. Alloys Compd.* **2017**, *695*, 818–826. [CrossRef]
30. Ghidiu, M.; Lukatskaya, M.R.; Zhao, M.Q.; Gogotsi, Y.; Barsoum, M.W. Conductive two-dimensional titanium carbide 'clay' with high volumetric capacitance. *Nature* **2014**, *516*, 78–81. [CrossRef]
31. Liu, F.F.; Zhou, J.; Wang, S.W.; Wang, B.X.; Shen, C.; Wang, L.B.; Hu, Q.K.; Huang, Q.; Zhou, A.G. Preparation of High-Purity V_2C MXene and Electrochemical Properties as Li-Ion Batteries. *J. Electrochem. Soc.* **2017**, *164*, A709–A713. [CrossRef]
32. Mashtalir, O.; Naguib, M.; Dyatkin, B.; Gogotsi, Y.; Barsoum, M.W. Kinetics of aluminum extraction from Ti_3AlC_2 in hydrofluoric acid. *Mater. Chem. Phys.* **2013**, *139*, 147–152. [CrossRef]
33. Halim, J.; Lukatskaya, M.R.; Cook, K.M.; Lu, J.; Smith, C.R.; Näslund, L.-Å.; May, S.J.; Hultman, L.; Gogotsi, Y.; Eklund, P.; et al. Transparent Conductive Two-Dimensional Titanium Carbide Epitaxial Thin Films. *Chem. Mater.* **2014**, *26*, 2374–2381. [CrossRef] [PubMed]
34. Urbankowski, P.; Anasori, B.; Makaryan, T.; Er, D.Q.; Kota, S.; Walsh, P.L.; Zhao, M.Q.; Shenoy, V.B.; Barsoum, M.W.; Gogotsi, Y. Synthesis of two-dimensional titanium nitride Ti_4N_3 (MXene). *Nanoscale* **2016**, *8*, 11385–11391. [CrossRef] [PubMed]
35. Shahzad, F.; Alhabeb, M.; Hatter, C.B.; Anasori, B.; Man Hong, S.; Koo, C.M.; Gogotsi, Y. Electromagnetic interference shielding with 2D transition metal carbides (MXenes). *Science* **2016**, *353*, 1137–1140. [CrossRef]
36. Mashtalir, O.; Naguib, M.; Mochalin, V.N.; Dall'Agnese, Y.; Heon, M.; Barsoum, M.W.; Gogotsi, Y. Intercalation and delamination of layered carbides and carbonitrides. *Nat. Commun.* **2013**, *4*, 1716. [CrossRef]
37. Naguib, M.; Unocic, R.R.; Armstrong, B.L.; Nanda, J. Large-scale delamination of multi-layers transition metal carbides and carbonitrides "MXenes". *Dalton Trans.* **2015**, *44*, 9353–9358. [CrossRef]
38. Mashtalir, O.; Lukatskaya, M.R.; Zhao, M.-Q.; Barsoum, M.W.; Gogotsi, Y. Amine-Assisted Delamination of Nb_2C MXene for Li-Ion Energy Storage Devices. *Adv. Mater.* **2015**, *27*, 3501–3506. [CrossRef]
39. Ma, R.; Sasaki, T. Two-Dimensional Oxide and Hydroxide Nanosheets: Controllable High-Quality Exfoliation, Molecular Assembly, and Exploration of Functionality. *Acc. Chem. Res.* **2015**, *48*, 136–143. [CrossRef]
40. Xu, M.; Lei, S.L.; Qi, J.; Dou, Q.Y.; Liu, L.Y.; Lu, Y.L.; Huang, Q.; Shi, S.Q.; Yan, X.B. Opening Magnesium Storage Capability of Two-Dimensional MXene by Intercalation of Cationic Surfactant. *ACS Nano* **2018**, *12*, 3733–3740. [CrossRef]
41. Alhabeb, M.; Maleski, K.; Anasori, B.; Lelyukh, P.; Clark, L.; Sin, S.; Gogotsi, Y. Guidelines for Synthesis and Processing of Two-Dimensional Titanium Carbide (Ti_3C_2Tx MXene). *Chem. Mater.* **2017**, *29*, 7633–7644. [CrossRef]
42. Li, T.; Yao, L.; Liu, Q.; Gu, J.; Luo, R.; Li, J.; Yan, X.; Wang, W.; Liu, P.; Chen, B.; et al. Fluorine-Free Synthesis of High-Purity Ti_3C_2Tx (T=OH, O) via Alkali Treatment. *Angew. Chem. Int. Ed.* **2018**, *57*, 6115–6119. [CrossRef]
43. Yang, S.; Zhang, P.P.; Wang, F.X.; Ricciardulli, A.G.; Lohe, M.R.; Blom, P.W.M.; Feng, X.L. Fluoride-Free Synthesis of Two-Dimensional Titanium Carbide (MXene) Using A Binary Aqueous System. *Angew. Chem. Int. Ed.* **2018**, *57*, 15491–15495. [CrossRef] [PubMed]
44. Sun, Z.; Yuan, M.; Lin, L.; Yang, H.; Nan, C.; Li, H.; Sun, G.; Yang, X. Selective Lithiation–Expansion–Microexplosion Synthesis of Two-Dimensional Fluoride-Free Mxene. *ACS Mater. Lett.* **2019**, *1*, 628–632. [CrossRef]

45. Li, M.; Lu, J.; Luo, K.; Li, Y.; Chang, K.; Chen, K.; Zhou, J.; Rosen, J.; Hultman, L.; Eklund, P.; et al. Element Replacement Approach by Reaction with Lewis Acidic Molten Salts to Synthesize Nanolaminated MAX Phases and MXenes. *J. Am. Chem. Soc.* **2019**, *141*, 4730–4737. [CrossRef]
46. Li, Y.B.; Shao, H.; Lin, Z.F.; Lu, J.; Liu, L.Y.; Duployer, B.; Persson, P.O.A.; Eklund, P.; Hultman, L.; Li, M.; et al. A general Lewis acidic etching route for preparing MXenes with enhanced electrochemical performance in non-aqueous electrolyte. *Nat. Mater.* **2020**, *19*, 894–899. [CrossRef]
47. Kamysbayev, V.; Filatov, A.S.; Hu, H.C.; Rui, X.; Lagunas, F.; Wang, D.; Klie, R.F.; Talapin, D.V. Covalent surface modifications and superconductivity of two-dimensional metal carbide MXenes. *Science* **2020**, *369*, 979–983. [CrossRef]
48. Chaitoglou, S.; Tsipas, P.; Speliotis, T.; Kordas, G.; Vavouliotis, A.; Dimoulas, A. Insight and control of the chemical vapor deposition growth parameters and morphological characteristics of graphene/Mo_2C heterostructures over liquid catalyst. *J. Cryst. Growth* **2018**, *495*, 46–53. [CrossRef]
49. Zhao, H.; Cai, K.; Ma, Z.; Cheng, Z.; Jia, T.; Kimura, H.; Fu, Q.; Tao, H.; Xiong, L. Synthesis of molybdenum carbide superconducting compounds by microwave-plasma chemical vapor deposition. *J. Appl. Phys.* **2018**, *123*, 053301. [CrossRef]
50. Meshkian, R.; Ingason, A.S.; Dahlqvist, M.; Petruhins, A.; Arnalds, U.B.; Magnus, F.; Lu, J.; Rosen, J. Theoretical stability, thin film synthesis and transport properties of the Mon +1GaCn MAX phase. *Phys. Status Solidi (RRL) Rapid Res. Lett.* **2015**, *9*, 197–201. [CrossRef]
51. Meshkian, R.; Näslund, L.-Å.; Halim, J.; Lu, J.; Barsoum, M.W.; Rosen, J. Synthesis of two-dimensional molybdenum carbide, Mo2C, from the gallium based atomic laminate Mo_2Ga_2C. *Scr. Mater.* **2015**, *108*, 147–150. [CrossRef]
52. Verger, L.; Natu, V.; Carey, M.; Barsoum, M.W. MXenes: An Introduction of Their Synthesis, Select Properties, and Applications. *Trends Chem.* **2019**, *1*, 656–669. [CrossRef]
53. Anasori, B.; Xie, Y.; Beidaghi, M.; Lu, J.; Hosler, B.C.; Hultman, L.; Kent, P.R.C.; Gogotsi, Y.; Barsoum, M.W. Two-Dimensional, Ordered, Double Transition Metals Carbides (MXenes). *ACS Nano* **2015**, *9*, 9507–9516. [CrossRef] [PubMed]
54. Zhang, C.J.; Pinilla, S.; McEvoy, N.; Cullen, C.P.; Anasori, B.; Long, E.; Park, S.-H.; Seral-Ascaso, A.; Shmeliov, A.; Krishnan, D.; et al. Oxidation Stability of Colloidal Two-Dimensional Titanium Carbides (MXenes). *Chem. Mater.* **2017**, *29*, 4848–4856. [CrossRef]
55. Xie, Y.; Dall'Agnese, Y.; Naguib, M.; Gogotsi, Y.; Barsoum, M.W.; Zhuang, H.L.; Kent, P.R.C. Prediction and Characterization of MXene Nanosheet Anodes for Non-Lithium-Ion Batteries. *ACS Nano* **2014**, *8*, 9606–9615. [CrossRef]
56. Wang, H.-W.; Naguib, M.; Page, K.; Wesolowski, D.J.; Gogotsi, Y. Resolving the Structure of Ti_3C_2Tx MXenes through Multilevel Structural Modeling of the Atomic Pair Distribution Function. *Chem. Mater.* **2016**, *28*, 349–359. [CrossRef]
57. Sun, N.; Guan, Z.R.X.; Zhu, Q.Z.; Anasori, B.; Gogotsi, Y.; Xu, B. Enhanced Ionic Accessibility of Flexible MXene Electrodes Produced by Natural Sedimentation. *Nano-Micro Lett.* **2020**, *12*, 89. [CrossRef]
58. Zhou, J.F.; Lin, S.; Huang, Y.N.; Tong, P.; Zhao, B.C.; Zhu, X.B.; Sun, Y.P. Synthesis and lithium ion storage performance of two-dimensional V_4C_3 MXene. *Chem. Eng. J.* **2019**, *373*, 203–212. [CrossRef]
59. Zhao, Q.; Zhu, Q.Z.; Miao, J.W.; Zhang, P.; Wan, P.B.; He, L.Z.; Xu, B. Flexible 3D Porous MXene Foam for High-Performance Lithium-Ion Batteries. *Small* **2019**, *15*, 1904293. [CrossRef]
60. Ren, C.E.; Zhao, M.-Q.; Makaryan, T.; Halim, J.; Boota, M.; Kota, S.; Anasori, B.; Barsoum, M.W.; Gogotsi, Y. Porous Two-Dimensional Transition Metal Carbide (MXene) Flakes for High-Performance Li-Ion Storage. *ChemElectroChem* **2016**, *3*, 689–693. [CrossRef]
61. Zhang, B.; Luo, C.; Zhou, G.; Pan, Z.-Z.; Ma, J.; Nishihara, H.; He, Y.-B.; Kang, F.; Lv, W.; Yang, Q.-H. Lamellar MXene Composite Aerogels with Sandwiched Carbon Nanotubes Enable Stable Lithium–Sulfur Batteries with a High Sulfur Loading. *Adv. Funct. Mater.* **2021**, *31*, 2100793. [CrossRef]
62. Guo, Z.; Zhou, J.; Si, C.; Sun, Z. Flexible two-dimensional $Ti_{n+1}C_n$ (n = 1, 2 and 3) and their functionalized MXenes predicted by density functional theories. *Phys. Chem. Chem. Phys.* **2015**, *17*, 15348–15354. [CrossRef] [PubMed]
63. Fu, Z.H.; Zhang, Q.F.; Legut, D.; Si, C.; Germann, T.C.; Lookman, T.; Du, S.Y.; Francisco, J.S.; Zhang, R.F. Stabilization and strengthening effects of functional groups in two-dimensional titanium carbide. *Phys. Rev. B* **2016**, *94*, 104103. [CrossRef]
64. Zha, X.-H.; Luo, K.; Li, Q.; Huang, Q.; He, J.; Wen, X.; Du, S. Role of the surface effect on the structural, electronic and mechanical properties of the carbide MXenes. *Europhys. Lett.* **2015**, *111*, 26007. [CrossRef]
65. Kurtoglu, M.; Naguib, M.; Gogotsi, Y.; Barsoum, M.W. First principles study of two-dimensional early transition metal carbides. *MRS Commun.* **2012**, *2*, 133–137. [CrossRef]
66. Plummer, G.; Anasori, B.; Gogotsi, Y.; Tucker, G.J. Nanoindentation of monolayer $Ti_{n+1}C_nTx$ MXenes via atomistic simulations: The role of composition and defects on strength. *Comput. Mater. Sci.* **2019**, *157*, 168–174. [CrossRef]
67. Si, C.; Jin, K.-H.; Zhou, J.; Sun, Z.; Liu, F. Large-Gap Quantum Spin Hall State in MXenes: D-Band Topological Order in a Triangular Lattice. *Nano Lett.* **2016**, *16*, 6584–6591. [CrossRef] [PubMed]
68. Dillon, A.D.; Ghidiu, M.J.; Krick, A.L.; Griggs, J.; May, S.J.; Gogotsi, Y.; Barsoum, M.W.; Fafarman, A.T. Highly Conductive Optical Quality Solution-Processed Films of 2D Titanium Carbide. *Adv. Funct. Mater.* **2016**, *26*, 4162–4168. [CrossRef]
69. Lai, S.; Jeon, J.; Jang, S.K.; Xu, J.; Choi, Y.J.; Park, J.-H.; Hwang, E.; Lee, S. Surface group modification and carrier transport properties of layered transition metal carbides (Ti_2CTx, T: -OH, -F and -O). *Nanoscale* **2015**, *7*, 19390–19396. [CrossRef]
70. Hantanasirisakul, K.; Gogotsi, Y. Electronic and Optical Properties of 2D Transition Metal Carbides and Nitrides (MXenes). *Adv. Mater.* **2018**, *30*, 1804779. [CrossRef]

71. Khazaei, M.; Ranjbar, A.; Arai, M.; Yunoki, S. Topological insulators in the ordered double transition metals $M'_2M''C_2$ MXenes (M′ = Mo, W; M″ = Ti, Zr, Hf). *Phys. Rev. B* **2016**, *94*, 125152. [CrossRef]
72. Khazaei, M.; Arai, M.; Sasaki, T.; Chung, C.-Y.; Venkataramanan, N.S.; Estili, M.; Sakka, Y.; Kawazoe, Y. Novel Electronic and Magnetic Properties of Two-Dimensional Transition Metal Carbides and Nitrides. *Adv. Funct. Mater.* **2013**, *23*, 2185–2192. [CrossRef]
73. Enyashin, A.N.; Ivanovskii, A.L. Two-dimensional titanium carbonitrides and their hydroxylated derivatives: Structural, electronic properties and stability of MXenes $Ti_3C_{2-}xNx(OH)_2$ from DFTB calculations. *J. Solid State Chem.* **2013**, *207*, 42–48. [CrossRef]
74. Li, X.; Zhu, Y.; Cai, W.; Borysiak, M.; Han, B.; Chen, D.; Piner, R.D.; Colombo, L.; Ruoff, R.S. Transfer of Large-Area Graphene Films for High-Performance Transparent Conductive Electrodes. *Nano Lett.* **2009**, *9*, 4359–4363. [CrossRef] [PubMed]
75. Xie, Y.; Naguib, M.; Mochalin, V.N.; Barsoum, M.W.; Gogotsi, Y.; Yu, X.Q.; Nam, K.W.; Yang, X.Q.; Kolesnikov, A.I.; Kent, P.R.C. Role of Surface Structure on Li-Ion Energy Storage Capacity of Two-Dimensional Transition-Metal Carbides. *J. Am. Chem. Soc.* **2014**, *136*, 6385–6394. [CrossRef] [PubMed]
76. Liu, X.B.A.; Shao, X.F.; Li, F.; Zhao, M.W. Anchoring effects of S-terminated Ti_2C MXene for lithium-sulfur batteries: A first-principles study. *Appl. Surf. Sci.* **2018**, *455*, 522–526. [CrossRef]
77. Hope, M.A.; Forse, A.C.; Griffith, K.J.; Lukatskaya, M.R.; Ghidiu, M.; Gogotsi, Y.; Grey, C.P. NMR reveals the surface functionalisation of Ti_3C_2 MXene. *Phys. Chem. Chem. Phys.* **2016**, *18*, 5099–5102. [CrossRef]
78. Persson, I.; Näslund, L.-Å.; Halim, J.; Barsoum, M.W.; Darakchieva, V.; Palisaitis, J.; Rosen, J.; Persson, P.O.Å. On the organization and thermal behavior of functional groups on Ti_3C_2 MXene surfaces in vacuum. *2D Mater.* **2018**, *5*, 015002. [CrossRef]
79. Tang, J.; Peng, X.; Lin, T.; Huang, X.; Luo, B.; Wang, L. Confining ultrafine tin monophosphide in Ti_3C_2Tx interlayers for rapid and stable sodium ion storage. *eScience* **2021**, *1*, 203–211. [CrossRef]
80. Jiang, M.; Fu, C.; Meng, P.; Ren, J.; Wang, J.; Bu, J.; Dong, A.; Zhang, J.; Xiao, W.; Sun, B. Challenges and Strategies of Low-Cost Aluminum Anodes for High-Performance Al-Based Batteries. *Adv. Mater.* **2022**, *34*, 2102026. [CrossRef]
81. Li, D.; Yuan, Y.; Liu, J.; Fichtner, M.; Pan, F. A review on current anode materials for rechargeable Mg batteries. *J. Magnes. Alloys* **2020**, *8*, 963–979. [CrossRef]
82. Liang, P.; Yi, J.; Liu, X.; Wu, K.; Wang, Z.; Cui, J.; Liu, Y.; Wang, Y.; Xia, Y.; Zhang, J. Highly Reversible Zn Anode Enabled by Controllable Formation of Nucleation Sites for Zn-Based Batteries. *Adv. Funct. Mater.* **2020**, *30*, 1908528. [CrossRef]
83. Chen, S.S.; Zhao, D.; Chen, L.; Liu, G.R.; Ding, Y.; Cao, Y.L.; Chen, Z.X. Emerging Intercalation Cathode Materials for Multivalent Metal-Ion Batteries: Status and Challenges. *Small Struct.* **2021**, *2*, 2100082. [CrossRef]
84. Wei, C.; Tan, L.; Zhang, Y.; Wang, Z.; Feng, J.; Qian, Y. Towards better Mg metal anodes in rechargeable Mg batteries: Challenges, strategies, and perspectives. *Energy Storage Mater.* **2022**, *52*, 299–319. [CrossRef]
85. Canepa, P.; Sai Gautam, G.; Hannah, D.C.; Malik, R.; Liu, M.; Gallagher, K.G.; Persson, K.A.; Ceder, G. Odyssey of Multivalent Cathode Materials: Open Questions and Future Challenges. *Chem. Rev.* **2017**, *117*, 4287–4341. [CrossRef]
86. Zhao, M.-Q.; Ren, C.E.; Alhabeb, M.; Anasori, B.; Barsoum, M.W.; Gogotsi, Y. Magnesium-Ion Storage Capability of MXenes. *ACS Appl. Energy Mater.* **2019**, *2*, 1572–1578. [CrossRef]
87. Gao, Q.; Come, J.; Naguib, M.; Jesse, S.; Gogotsi, Y.; Balke, N. Synergetic effects of K^+ and Mg^{2+} ion intercalation on the electrochemical and actuation properties of the two-dimensional Ti_3C_2 MXene. *Faraday Discuss.* **2017**, *199*, 393–403. [CrossRef]
88. Liu, F.F.; Liu, Y.C.; Zhao, X.D.; Liu, X.B.; Fan, L.Z. Pursuit of a high-capacity and long-life Mg-storage cathode by tailoring sandwich-structured MXene@carbon nanosphere composites. *J. Mater. Chem. A* **2019**, *7*, 16712–16719. [CrossRef]
89. Xu, M.; Bai, N.; Li, H.-X.; Hu, C.; Qi, J.; Yan, X.-B. Synthesis of MXene-supported layered MoS_2 with enhanced electrochemical performance for Mg batteries. *Chin. Chem. Lett.* **2018**, *29*, 1313–1316. [CrossRef]
90. Li, Y.; Xu, D.; Zhang, D.; Wei, Y.; Qu, D.; Guo, Y. Study on MXene-supported Layered TiS_2 as Cathode Materials for Magnesium Batteries. *Int. J. Electrochem. Sci.* **2019**, *14*, 11102–11109. [CrossRef]
91. Liu, F.F.; Wang, T.T.; Liu, X.B.; Jiang, N.; Fan, L.Z. High-performance heterojunction $Ti_3C_2/CoSe_2$ with both intercalation and conversion storage mechanisms for magnesium batteries. *Chem. Eng. J.* **2021**, *426*, 130747. [CrossRef]
92. Zhu, J.L.; Zhang, X.; Gao, H.G.; Shao, Y.T.; Liu, Y.N.; Zhu, Y.F.; Zhang, J.G.; Li, L.Q. VS_4 anchored on Ti_3C_2 MXene as a high-performance cathode material for magnesium ion battery. *J. Power Sources* **2022**, *518*, 230731. [CrossRef]
93. Yang, C.; Yang, L.; Chai, Z.; Zheng, X.; Li, J.; Yang, Y.; Zhu, J.; Jin, X.; Li, Q.; Xu, D. Alternate-stacked $Li_4Ti_5O_{12}$ nanosheets/d-Ti_3C_2 flexible film as a current collector-free, high-capacity and robust cathode for rechargeable Mg batteries. *Nano Sel.* **2020**, *1*, 1–11. [CrossRef]
94. Li, Y.; Zhang, R.N.; Xu, D.H.; Zhang, D.H.; Wei, Y.C.; Guo, Y.X. Study on MnO_2/MXene-V_2C composite as cathode for magnesium ion battery. *Int. J. Electrochem. Sci.* **2020**, *15*, 11227–11237. [CrossRef]
95. Chen, J.; Xiao, B.Q.; Hu, C.F.; Chen, H.D.; Huang, J.J.; Yan, D.; Peng, S.L. Construction Strategy of VO_2@V_2C 1D/2D Heterostructure and Improvement of Zinc-Ion Diffusion Ability in VO_2 (B). *ACS Appl. Mater. Interfaces* **2022**, *14*, 28760–28768. [CrossRef]
96. Chen, C.; Xie, X.Q.; Anasori, B.; Sarycheva, A.; Makaryan, T.; Zhao, M.Q.; Urbankowski, P.; Miao, L.; Jiang, J.J.; Gogotsi, Y. MoS_2-on-MXene Heterostructures as Highly Reversible Anode Materials for Lithium-Ion Batteries. *Angew. Chem. Int. Ed.* **2018**, *57*, 1846–1850. [CrossRef]
97. Sha, D.W.; Lu, C.J.; He, W.; Ding, J.X.; Zhang, H.; Bao, Z.H.; Cao, X.; Fan, J.C.; Dou, Y.; Pan, L.; et al. Surface Selenization Strategy for V_2CTx MXene toward Superior Zn-Ion Storage. *ACS Nano* **2022**, *16*, 2711–2720. [CrossRef]

98. Gao, P.; Shi, H.; Ma, T.; Liang, S.; Xia, Y.; Xu, Z.; Wang, S.; Min, C.; Liu, L. MXene/TiO_2 Heterostructure-Decorated Hard Carbon with Stable Ti–O–C Bonding for Enhanced Sodium-Ion Storage. *ACS Appl. Mater. Interfaces* **2021**, *13*, 51028–51038. [CrossRef]
99. Zhao, D.; Chen, S.; Lai, Y.; Ding, M.; Cao, Y.; Chen, Z. A stable "rocking-chair" zinc-ion battery boosted by low-strain $Zn_3V_4(PO_4)_6$ cathode. *Nano Energy* **2022**, *100*, 107520. [CrossRef]
100. Shi, M.J.; Wang, B.; Chen, C.; Lang, J.W.; Yan, C.; Yan, X.B. 3D high-density MXene@MnO_2 microflowers for advanced aqueous zinc-ion batteries. *J. Mater. Chem. A* **2020**, *8*, 24635–24644. [CrossRef]
101. Ahmed, B.; Anjum, D.H.; Gogotsi, Y.; Alshareef, H.N. Atomic layer deposition of SnO_2 on MXene for Li-ion battery anodes. *Nano Energy* **2017**, *34*, 249–256. [CrossRef]
102. Byeon, A.; Zhao, M.Q.; Ren, C.E.; Halim, J.; Kota, S.; Urbankowski, P.; Anasori, B.; Barsoum, M.W.; Gogotsi, Y. Two-Dimensional Titanium Carbide MXene As a Cathode Material for Hybrid Magnesium/Lithium-Ion Batteries. *ACS Appl. Mater. Interfaces* **2017**, *9*, 4296–4300. [CrossRef]
103. Liu, F.F.; Liu, Y.C.; Zhao, X.D.; Liu, K.Y.; Yin, H.Q.; Fan, L.Z. Prelithiated V_2C MXene: A High-Performance Electrode for Hybrid Magnesium/Lithium-Ion Batteries by Ion Cointercalation. *Small* **2020**, *16*, 1906076. [CrossRef]
104. Li, X.H.; Tang, Y.K.; Liu, L.; Zhang, Y.; Sheng, R.; NuLi, Y.N. Ti_3C_2 MXene with pillared structure for hybrid magnesium-lithium batteries cathode material with long cycle life and high rate capability. *J. Colloid Interface Sci.* **2022**, *608*, 2455–2462. [CrossRef]
105. Yu, L.; Zhang, X. Electrochemical insertion of magnesium ions into V_2O_5 from aprotic electrolytes with varied water content. *J. Colloid Interface Sci.* **2004**, *278*, 160–165. [CrossRef]
106. Du, A.; Zhang, Z.; Qu, H.; Cui, Z.; Qiao, L.; Wang, L.; Chai, J.; Lu, T.; Dong, S.; Dong, T.; et al. An efficient organic magnesium borate-based electrolyte with non-nucleophilic characteristics for magnesium–sulfur battery. *Energy Environ. Sci.* **2017**, *10*, 2616–2625. [CrossRef]
107. Zhang, R.; Yu, X.; Nam, K.-W.; Ling, C.; Arthur, T.S.; Song, W.; Knapp, A.M.; Ehrlich, S.N.; Yang, X.-Q.; Matsui, M. α-MnO_2 as a cathode material for rechargeable Mg batteries. *Electrochem. Commun.* **2012**, *23*, 110–113. [CrossRef]
108. Zhang, E.; Cao, W.; Wang, B.; Yu, X.; Wang, L.; Xu, Z.; Lu, B. A novel aluminum dual-ion battery. *Energy Storage Mater.* **2018**, *11*, 91–99. [CrossRef]
109. Mohandas, K.S.; Sanil, N.; Noel, M.; Rodriguez, P. Electrochemical intercalation of aluminium chloride in graphite in the molten sodium chloroaluminate medium. *Carbon* **2003**, *41*, 927–932. [CrossRef]
110. Yang, H.; Li, H.; Li, J.; Sun, Z.; He, K.; Cheng, H.-M.; Li, F. The Rechargeable Aluminum Battery: Opportunities and Challenges. *Angew. Chem. Int. Ed.* **2019**, *58*, 11978–11996. [CrossRef]
111. VahidMohammadi, A.; Hadjikhani, A.; Shahbazmohamadi, S.; Beidaghi, M. Two-Dimensional Vanadium Carbide (MXene) as a High-Capacity Cathode Material for Rechargeable Aluminum Batteries. *ACS Nano* **2017**, *11*, 11135–11144. [CrossRef] [PubMed]
112. Lee, S.; Jung, S.C.; Han, Y.K. Fe_2CS_2 MXene: A promising electrode for Al-ion batteries. *Nanoscale* **2020**, *12*, 5324–5331. [CrossRef] [PubMed]
113. Li, Z.Y.; Wang, X.X.; Zhang, W.M.; Yang, S.P. Two-dimensional Ti_3C_2@CTAB-Se (MXene) composite cathode material for high-performance rechargeable aluminum batteries. *Chem. Eng. J.* **2020**, *398*, 125679. [CrossRef]
114. Huo, X.G.; Wang, X.X.; Li, Z.Y.; Liu, J.; Li, J.L. Two-dimensional composite of D-Ti_3C_2Tx@S@TiO_2 (MXene) as the cathode material for aluminum-ion batteries. *Nanoscale* **2020**, *12*, 3387–3399. [CrossRef] [PubMed]
115. Monti, D.; Ponrouch, A.; Araujo, R.B.; Barde, F.; Johansson, P.; Palacín, M.R. Multivalent Batteries—Prospects for High Energy Density: Ca Batteries. *Front. Chem.* **2019**, *7*, 79. [CrossRef]
116. Aurbach, D.; Skaletsky, R.; Gofer, Y. The Electrochemical Behavior of Calcium Electrodes in a Few Organic Electrolytes. *J. Electrochem. Soc.* **1991**, *138*, 3536. [CrossRef]
117. Ponrouch, A.; Frontera, C.; Bardé, F.; Palacín, M.R. Towards a calcium-based rechargeable battery. *Nat. Mater.* **2016**, *15*, 169–172. [CrossRef]
118. Dinda, P.P.; Meena, S. A V_3C_2 MXene/graphene heterostructure as a sustainable electrode material for metal ion batteries. *J. Phys. Condens. Matter* **2021**, *33*, 175001. [CrossRef]
119. Demiroglu, I.; Peeters, F.M.; Gulseren, O.; Cakir, D.; Sevik, C. Alkali Metal Intercalation in MXene/Graphene Heterostructures: A New Platform for Ion Battery Applications. *J. Phys. Chem. Lett.* **2019**, *10*, 727–734. [CrossRef]
120. Wang, Y.Z.; Ma, Y.H.; Zhang, Q.F.; Huang, R.; Gao, B.L.; Li, Z.W.; Li, G.N.; Liang, F. First-principles investigation of V_2CSe_2 MXene as a potential anode material for non-lithium metal ion batteries. *Curr. Appl. Phys.* **2022**, *41*, 7–13. [CrossRef]
121. Ma, L.; Zhi, C. Zn electrode/electrolyte interfaces of Zn batteries: A mini review. *Electrochem. Commun.* **2021**, *122*, 106898. [CrossRef]
122. Wang, T.; Li, C.; Xie, X.; Lu, B.; He, Z.; Liang, S.; Zhou, J. Anode Materials for Aqueous Zinc Ion Batteries: Mechanisms, Properties, and Perspectives. *ACS Nano* **2020**, *14*, 16321–16347. [CrossRef] [PubMed]
123. Yufit, V.; Tariq, F.; Eastwood, D.S.; Biton, M.; Wu, B.; Lee, P.D.; Brandon, N.P. Operando Visualization and Multi-scale Tomography Studies of Dendrite Formation and Dissolution in Zinc Batteries. *Joule* **2019**, *3*, 485–502. [CrossRef]
124. Li, H.F.; Ma, L.T.; Han, C.P.; Wang, Z.F.; Liu, Z.X.; Tang, Z.J.; Zhi, C.Y. Advanced rechargeable zinc-based batteries: Recent progress and future perspectives. *Nano Energy* **2019**, *62*, 550–587. [CrossRef]
125. Tian, Y.; An, Y.L.; Wei, C.L.; Xi, B.J.; Xiong, S.L.L.; Feng, J.K.; Qian, Y.T. Flexible and Free-Standing Ti_3C_2Tx MXene@Zn Paper for Dendrite-Free Aqueous Zinc Metal Batteries and Nonaqueous Lithium Metal Batteries. *ACS Nano* **2019**, *13*, 11676–11685. [CrossRef]
126. Zhou, J.H.; Xie, M.; Wu, F.; Mei, Y.; Hao, Y.T.; Li, L.; Chen, R.J. Encapsulation of Metallic Zn in a Hybrid MXene/Graphene Aerogel as a Stable Zn Anode for Foldable Zn-Ion Batteries. *Adv. Mater.* **2022**, *34*, 2106897. [CrossRef]

127. Liu, H.; Ma, Y.; Cao, B.; Zhu, Q.; Xu, B. Recent Progress of MXenes in Aqueous Zinc-Ion Batteries. *Acta Phys. Chim. Sin.* **2023**, *39*, 2210027. [CrossRef]
128. Li, X.L.; Li, Q.; Hou, Y.; Yang, Q.; Chen, Z.; Huang, Z.D.; Liang, G.J.; Zhao, Y.W.; Ma, L.T.; Li, M.A.; et al. Toward a Practical Zn Powder Anode: Ti_3C_2Tx MXene as a Lattice-Match Electrons/Ions Redistributor. *ACS Nano* **2021**, *15*, 14631–14642. [CrossRef]
129. Tang, B.; Shan, L.; Liang, S.; Zhou, J. Issues and opportunities facing aqueous zinc-ion batteries. *Energy Environ. Sci.* **2019**, *12*, 3288–3304. [CrossRef]
130. Zhang, N.N.; Huang, S.; Yuan, Z.S.; Zhu, J.C.; Zhao, Z.F.; Niu, Z.Q. Direct Self-Assembly of MXene on Zn Anodes for Dendrite-Free Aqueous Zinc-Ion Batteries. *Angew. Chem. Int. Ed.* **2021**, *60*, 2861–2865. [CrossRef]
131. Li, X.L.; Li, M.A.; Luo, K.; Hou, Y.; Li, P.; Yang, Q.; Huang, Z.D.; Liang, G.J.; Chen, Z.; Du, S.Y.; et al. Lattice Matching and Halogen Regulation for Synergistically Induced Uniform Zinc Electrodeposition by Halogenated Ti_3C_2 MXenes. *ACS Nano* **2022**, *16*, 813–822. [CrossRef] [PubMed]
132. Sun, K.; Shen, Y.; Min, J.; Pang, J.; Zheng, Y.; Gu, T.; Wang, G.; Chen, L. MOF-derived Zn/Co co-doped MnO/C microspheres as cathode and Ti_3C_2@Zn as anode for aqueous zinc-ion full battery. *Chem. Eng. J.* **2023**, *454*, 140394. [CrossRef]
133. An, Y.; Tian, Y.; Liu, C.; Xiong, S.; Feng, J.; Qian, Y. Rational Design of Sulfur-Doped Three-Dimensional Ti_3C_2Tx MXene/ZnS Heterostructure as Multifunctional Protective Layer for Dendrite-Free Zinc-Ion Batteries. *ACS Nano* **2021**, *15*, 15259–15273. [CrossRef] [PubMed]
134. Tan, L.; Wei, C.; Zhang, Y.; An, Y.; Xiong, S.; Feng, J. Long-life and dendrite-free zinc metal anode enabled by a flexible, green and self-assembled zincophilic biomass engineered MXene based interface. *Chem. Eng. J.* **2022**, *431*, 134277. [CrossRef]
135. Tian, Y.; An, Y.; Liu, C.; Xiong, S.; Feng, J.; Qian, Y. Reversible zinc-based anodes enabled by zincophilic antimony engineered MXene for stable and dendrite-free aqueous zinc batteries. *Energy Storage Mater.* **2021**, *41*, 343–353. [CrossRef]
136. Wang, X.; Wang, Y.M.; Jiang, Y.P.; Li, X.L.; Liu, Y.; Xiao, H.H.; Ma, Y.; Huang, Y.Y.; Yuan, G.H. Tailoring Ultrahigh Energy Density and Stable Dendrite-Free Flexible Anode with Ti_3C_2Tx MXene Nanosheets and Hydrated Ammonium Vanadate Nanobelts for Aqueous Rocking-Chair Zinc Ion Batteries. *Adv. Funct. Mater.* **2021**, *31*, 2103210. [CrossRef]
137. Zhao, B.; Wang, S.; Yu, Q.; Wang, Q.; Wang, M.; Ni, T.; Ruan, L.; Zeng, W. A flexible, heat-resistant and self-healable "rocking-chair" zinc ion microbattery based on MXene-TiS_2 (de)intercalation anode. *J. Power Sources* **2021**, *504*, 230076. [CrossRef]
138. Sun, C.; Wu, C.; Gu, X.; Wang, C.; Wang, Q. Interface Engineering via Ti_3C_2Tx MXene Electrolyte Additive toward Dendrite-Free Zinc Deposition. *Nano-Micro Lett.* **2021**, *13*, 89. [CrossRef]
139. Chen, Z.; Li, X.; Wang, D.; Yang, Q.; Ma, L.; Huang, Z.; Liang, G.; Chen, A.; Guo, Y.; Dong, B.; et al. Grafted MXene/polymer electrolyte for high performance solid zinc batteries with enhanced shelf life at low/high temperatures. *Energy Environ. Sci.* **2021**, *14*, 3492–3501. [CrossRef]
140. Wang, S.; Wang, Q.; Zeng, W.; Wang, M.; Ruan, L.; Ma, Y. A New Free-Standing Aqueous Zinc-Ion Capacitor Based on MnO_2–CNTs Cathode and MXene Anode. *Nano-Micro Lett.* **2019**, *11*, 70. [CrossRef]
141. Shi, J.; Wang, S.; Wang, Q.; Chen, X.; Du, X.; Wang, M.; Zhao, Y.; Dong, C.; Ruan, L.; Zeng, W. A new flexible zinc-ion capacitor based on δ-MnO_2@Carbon cloth battery-type cathode and MXene@Cotton cloth capacitor-type anode. *J. Power Sources* **2020**, *446*, 227345. [CrossRef]
142. Huang, L.; Lin, Y.; Zeng, W.; Xu, C.; Chen, Z.; Wang, Q.; Zhou, H.; Yu, Q.; Zhao, B.; Ruan, L.; et al. Highly Transparent and Flexible Zn-Ti_3C_2Tx MXene Hybrid Capacitors. *Langmuir* **2022**, *38*, 5968–5976. [CrossRef] [PubMed]
143. Jin, Y.; Ao, H.; Qi, K.; Zhang, X.; Liu, M.; Zhou, T.; Wang, S.; Xia, G.; Zhu, Y. A High-rate, Long Life, and Anti-self-discharge Aqueous N-doped Ti_3C_2/Zn Hybrid Capacitor. *Mater. Today Energy* **2021**, *19*, 100598. [CrossRef]
144. Wang, Q.; Wang, S.L.; Guo, X.H.; Ruan, L.M.; Wei, N.; Ma, Y.; Li, J.Y.; Wang, M.; Li, W.Q.; Zeng, W. MXene-Reduced Graphene Oxide Aerogel for Aqueous Zinc-Ion Hybrid Supercapacitor with Ultralong Cycle Life. *Adv. Electron. Mater.* **2019**, *5*, 1900537. [CrossRef]
145. Wang, C.D.; Wei, S.Q.; Chen, S.M.; Cao, D.F.; Song, L. Delaminating Vanadium Carbides for Zinc-Ion Storage: Hydrate Precipitation and H^+/Zn^{2+} Co-Action Mechanism. *Small Methods* **2019**, *3*, 1900495. [CrossRef]
146. Maughan, P.A.; Tapia-Ruiz, N.; Bimbo, N. In-situ pillared MXene as a viable zinc-ion hybrid capacitor. *Electrochim. Acta* **2020**, *341*, 136061. [CrossRef]
147. Fan, Z.; Jin, J.; Li, C.; Cai, J.; Wei, C.; Shao, Y.; Zou, G.; Sun, J. 3D-Printed Zn-Ion Hybrid Capacitor Enabled by Universal Divalent Cation-Gelated Additive-Free Ti_3C_2 MXene Ink. *ACS Nano* **2021**, *15*, 3098–3107. [CrossRef]
148. Li, Z.; Guo, D.; Wang, D.; Sun, M.; Sun, H. Exploration of Metal/Ti3C2 MXene-derived composites as anode for high-performance zinc-ion supercapacitor. *J. Power Sources* **2021**, *506*, 230197. [CrossRef]
149. Yang, Q.; Huang, Z.; Li, X.; Liu, Z.; Li, H.; Liang, G.; Wang, D.; Huang, Q.; Zhang, S.; Chen, S.; et al. A Wholly Degradable, Rechargeable Zn–Ti3C2 MXene Capacitor with Superior Anti-Self-Discharge Function. *ACS Nano* **2019**, *13*, 8275–8283. [CrossRef]
150. Luo, S.J.; Xie, L.Y.; Han, F.; Wei, W.; Huang, Y.; Zhang, H.; Zhu, M.S.; Schmidt, O.G.; Wang, L. Nanoscale Parallel Circuitry Based on Interpenetrating Conductive Assembly for Flexible and High-Power Zinc Ion Battery. *Adv. Funct. Mater.* **2019**, *29*, 1901336. [CrossRef]
151. Shi, M.; Wang, B.; Shen, Y.; Jiang, J.; Zhu, W.; Su, Y.; Narayanasamy, M.; Angaiah, S.; Yan, C.; Peng, Q. 3D assembly of MXene-stabilized spinel $ZnMn_2O_4$ for highly durable aqueous zinc-ion batteries. *Chem. Eng. J.* **2020**, *399*, 125627. [CrossRef]
152. Zhu, X.; Cao, Z.; Wang, W.; Li, H.; Dong, J.; Gao, S.; Xu, D.; Li, L.; Shen, J.; Ye, M. Superior-Performance Aqueous Zinc-Ion Batteries Based on the In Situ Growth of MnO_2 Nanosheets on V2CTX MXene. *ACS Nano* **2021**, *15*, 2971–2983. [CrossRef] [PubMed]
153. Xu, G.; Zhang, Y.; Gong, Z.; Lu, T.; Pan, L. Three-dimensional hydrated vanadium pentoxide/MXene composite for high-rate zinc-ion batteries. *J. Colloid Interface Sci.* **2021**, *593*, 417–423. [CrossRef] [PubMed]

154. Huang, J.; Zhou, J.; Liang, S. Guest pre-intercalation strategy to boost the electrochemical performance of aqueous zinc-ion battery cathodes. *Acta Phys. Chim. Sin.* **2021**, *37*, 2005020. [CrossRef]
155. Liu, C.; Xu, W.; Mei, C.; Li, M.-C.; Xu, X.; Wu, Q. Highly stable $H_2V_3O_8$/Mxene cathode for Zn-ion batteries with superior rate performance and long lifespan. *Chem. Eng. J.* **2021**, *405*, 126737. [CrossRef]
156. Shi, Z.; Ru, Q.; Pan, Z.; Zheng, M.; Chi-Chun Ling, F.; Wei, L. Flexible Free-Standing VO_2/MXene Conductive Films as Cathodes for Quasi-Solid-State Zinc-Ion Batteries. *ChemElectroChem* **2021**, *8*, 1091–1097. [CrossRef]
157. Liu, H.; Jiang, L.; Cao, B.; Du, H.; Lu, H.; Ma, Y.; Wang, H.; Guo, H.; Huang, Q.; Xu, B.; et al. Van der Waals Interaction-Driven Self-Assembly of V_2O_5 Nanoplates and MXene for High-Performing Zinc-Ion Batteries by Suppressing Vanadium Dissolution. *ACS Nano* **2022**, *16*, 14539–14548. [CrossRef]
158. Li, X.; Li, M.; Yang, Q.; Li, H.; Xu, H.; Chai, Z.; Chen, K.; Liu, Z.; Tang, Z.; Ma, L.; et al. Phase Transition Induced Unusual Electrochemical Performance of V_2CTX MXene for Aqueous Zinc Hybrid-Ion Battery. *ACS Nano* **2020**, *14*, 541–551. [CrossRef]
159. Liu, Y.; Jiang, Y.; Hu, Z.; Peng, J.; Lai, W.; Wu, D.; Zuo, S.; Zhang, J.; Chen, B.; Dai, Z.; et al. In-Situ Electrochemically Activated Surface Vanadium Valence in V_2C MXene to Achieve High Capacity and Superior Rate Performance for Zn-Ion Batteries. *Adv. Funct. Mater.* **2021**, *31*, 2008033. [CrossRef]
160. Narayanasamy, M.; Kirubasankar, B.; Shi, M.; Velayutham, S.; Wang, B.; Angaiah, S.; Yan, C. Morphology restrained growth of V_2O_5 by the oxidation of V-MXenes as a fast diffusion controlled cathode material for aqueous zinc ion batteries. *Chem. Commun.* **2020**, *56*, 6412–6415. [CrossRef]
161. Tian, Y.; An, Y.; Wei, H.; Wei, C.; Tao, Y.; Li, Y.; Xi, B.; Xiong, S.; Feng, J.; Qian, Y. Micron-Sized Nanoporous Vanadium Pentoxide Arrays for High-Performance Gel Zinc-Ion Batteries and Potassium Batteries. *Chem. Mater.* **2020**, *32*, 4054–4064. [CrossRef]
162. Venkatkarthick, R.; Rodthongkum, N.; Zhang, X.; Wang, S.; Pattananuwat, P.; Zhao, Y.; Liu, R.; Qin, J. Vanadium-Based Oxide on Two-Dimensional Vanadium Carbide MXene (V_2Ox@V_2CTx) as Cathode for Rechargeable Aqueous Zinc-Ion Batteries. *ACS Appl. Energy Mater.* **2020**, *3*, 4677–4689. [CrossRef]
163. Zhu, X.; Wang, W.; Cao, Z.; Gao, S.; Chee, M.O.L.; Zhang, X.; Dong, P.; Ajayan, P.M.; Ye, M.; Shen, J. Zn^{2+}-Intercalated $V_2O_5 \cdot nH_2O$ derived from V_2CTx MXene for hyper-stable zinc-ion storage. *J. Mater. Chem. A* **2021**, *9*, 17994–18005. [CrossRef]
164. Zhu, X.; Cao, Z.; Li, X.-L.; Pei, L.; Jones, J.; Zhou, Y.-N.; Dong, P.; Wang, L.; Ye, M.; Shen, J. Ion-intercalation regulation of MXene-derived hydrated vanadates for high-rate and long-life Zn-Ion batteries. *Energy Storage Mater.* **2022**, *45*, 568–577. [CrossRef]
165. Dong, C.; Xu, F.; Chen, L.; Chen, Z.; Cao, Y. Design Strategies for High-Voltage Aqueous Batteries. *Small Struct.* **2021**, *2*, 2100001. [CrossRef]
166. Li, X.; Li, M.; Yang, Q.; Liang, G.; Huang, Z.; Ma, L.; Wang, D.; Mo, F.; Dong, B.; Huang, Q.; et al. In Situ Electrochemical Synthesis of MXenes without Acid/Alkali Usage in/for an Aqueous Zinc Ion Battery. *Adv. Energy Mater.* **2020**, *10*, 2001791. [CrossRef]
167. Long, F.; Zhang, Q.; Shi, J.; Wen, L.; Wu, Y.; Ren, Z.; Liu, Z.; Hou, Y.; Mao, K.; Niu, K.; et al. Ultrastable and ultrafast 3D charge–discharge network of robust chemically coupled 1 T-MoS_2/Ti_3C_2 MXene heterostructure for aqueous Zn-ion batteries. *Chem. Eng. J.* **2022**, *455*, 140539. [CrossRef]
168. Shi, J.; Hou, Y.; Liu, Z.; Zheng, Y.; Wen, L.; Su, J.; Li, L.; Liu, N.; Zhang, Z.; Gao, Y. The high-performance MoO_{3-x}/MXene cathodes for zinc-ion batteries based on oxygen vacancies and electrolyte engineering. *Nano Energy* **2022**, *91*, 106651. [CrossRef]
169. Zhang, Y.; Cao, J.; Li, J.; Yuan, Z.; Li, D.; Wang, L.; Han, W. Self-assembled Cobalt-doped NiMn-layered double hydroxide (LDH)/V_2CTx MXene hybrids for advanced aqueous electrochemical energy storage properties. *Chem. Eng. J.* **2022**, *430*, 132992. [CrossRef]
170. Liu, Y.; Dai, Z.; Zhang, W.; Jiang, Y.; Peng, J.; Wu, D.; Chen, B.; Wei, W.; Chen, X.; Liu, Z.; et al. Sulfonic-Group-Grafted Ti_3C_2Tx MXene: A Silver Bullet to Settle the Instability of Polyaniline toward High-Performance Zn-Ion Batteries. *ACS Nano* **2021**, *15*, 9065–9075. [CrossRef]
171. Li, X.; Ma, X.; Hou, Y.; Zhang, Z.; Lu, Y.; Huang, Z.; Liang, G.; Li, M.; Yang, Q.; Ma, J.; et al. Intrinsic voltage plateau of a Nb_2CTx MXene cathode in an aqueous electrolyte induced by high-voltage scanning. *Joule* **2021**, *5*, 2993–3005. [CrossRef]
172. Li, M.; Li, X.; Qin, G.; Luo, K.; Lu, J.; Li, Y.; Liang, G.; Huang, Z.; Zhou, J.; Hultman, L.; et al. Halogenated Ti_3C_2 MXenes with Electrochemically Active Terminals for High-Performance Zinc Ion Batteries. *ACS Nano* **2021**, *15*, 1077–1085. [CrossRef] [PubMed]